A kinetic model for simulating non-equilibrium mass transport in oxides applied to hematite growth under irradiation

Kohnert, Aaron Anthony
Holby, Edward F.
Peterson, Elizabeth Ann
Srivastava, Shivani
Asta, Mark D.
Uberuaga, Blas P.

To be published in: Corrosion Science

DOI to publisher's version: 10.1016/j.corsci.2026.113709

Journal Pre-proof

A kinetic model for simulating non-equilibrium mass transport in oxides applied to hematite growth under irradiation

Aaron A. Kohnert, Edward F. Holby, Elizabeth A. Peterson,
Shivani Srivastava, Mark Asta, Blas P. Uberuaga

PII: S0010-938X(26)00118-6
DOI: https://doi.org/10.1016/j.corsci.2026.113709
Reference: CS 113709

To appear in: *Corrosion Science*

Received date : 5 November 2025
Revised date : 29 January 2026
Accepted date : 12 February 2026

Please cite this article as: A.A. Kohnert, E.F. Holby, E.A. Peterson et al., A kinetic model for simulating non-equilibrium mass transport in oxides applied to hematite growth under irradiation, *Corrosion Science* (2026), doi: https://doi.org/10.1016/j.corsci.2026.113709.

Revised Manuscript (Clean Version)

A Kinetic Model for Simulating Non-Equilibrium Mass Transport in Oxides Applied to Hematite Growth Under Irradiation

Aaron A Kohnert[a,*], Edward F Holby[b], Elizabeth A Peterson[b], Shivani Srivastava[c], Mark Asta[c], Blas P Uberuaga[a]

[a]*Los Alamos National Laboratory, Materials Science and Technology Division, PO Box 1663, Los Alamos, 87545, NM, USA*
[b]*Los Alamos National Laboratory, Theoretical Division, PO Box 1663, Los Alamos, 87545, NM, USA*
[c]*University of California Berkeley, Department of Materials Science and Engineering, 210 Hearst Memorial Mining Building, Berkeley, 94720, CA, USA*

Abstract

We propose an approach to simulating the dynamic evolution and transport of charged point defects within and through the oxide scales that form during corrosion. The method follows the cluster dynamics formalism widely adopted for radiation damage in solids, which can apply in both quasi-static and far from equilibrium conditions, such as in radiation environments. By treating each charged defect as a cluster of an atomic defect and associated unit charges, the proposed model flexibly allows charge state transitions and shifts in the Fermi level by absorption and emission of charge carriers from point defects in a reaction network with rates constrained by local equilibrium. Applying this model to hematite predicts changes in self-diffusion and oxidation kinetics in irradiation environments, surprisingly showing reduced oxidation rates in many conditions, despite enhanced self-diffusion. The origin of this effect lies in a change in Fermi level induced by excess vacancies formed under irradiation, which in turn suppresses the transport of cation interstitials which facilitate hematite growth.

1. Introduction

Mass transport through crystalline solids is mediated by the presence and migration of defects in the crystal. Point defects in the lattice structure, such as atoms which are missing from a lattice site (vacancies) or extra atoms which sit between or doubly occupy lattice sites (interstitials) can transition from site to site, allowing atoms to move through the solid. Point defect transport kinetics through oxides are of particular technological importance. For example, oxides are particularly attractive as fast ion conductors [1]. In non-equilibrium environments, understanding radiation effects in functional oxides such as Ga_2O_3 requires knowing the kinetics of point defects[2]. Similarly, the evolution of nuclear fuels such as UO_2 is dictated by point defect and defect cluster transport [3]. The process of forming stable oxide scales on a metal surface is critically important in protecting the metal from further corrosion and from the ingress of embrittling contaminants such as hydrogen and carbon[4]. Critical components of the energy infrastructure such as turbines, reactors, and heat exchangers require structural materials where such scales form to protect the base metal, but also do not experience oxidation so rapid that it becomes ineffective to prevent further corrosion through fracture and spallation.

Oxide growth requires either inward transport of oxygen to the underlying metal, or outward transport of metal to the oxidizing environment (or both), mediated by point defect migration. The conditions under which corrosion occurs are highly non-equilibrium, and the extreme environments relevant to the energy infrastructure are often expensive and complicated to replicate in laboratory environments, even more so for nuclear reactor conditions. To facilitate understanding corrosion in these scenarios, we advance a generalized model describing the growth of oxide scales in terms of the coupled kinetics of point defect transport, with specific application to the growth of α-Fe_2O_3 (hematite) in both thermal and radiation environments.

Several well-established models based on the migration of ions (interstitial atoms) or vacant lattice sites through the oxide are in regular use, each invoking different individual mechanisms and driving forces for mass transport[5]. These models have individually rationalized the empirically observed logarithmic-type growth behavior at small thicknesses and low temperatures[6, 7, 8, 9, 10] and quadratic growth with an Arrhenius temperature dependence for thicker scales[11]. The dominant species facilitating growth can be either the anion or cation, with either vacancy or interstitial type defects as the vehicle for the flux of those atoms. These possibilities each provide different dependencies on oxidizing environment and temperature, with the possibility that a mechanism inactive in one set of conditions governs the kinetics in a different set of conditions. To further complicate matters, exposure to radiation produces point defects athermally throughout the oxide scale (rather than thermally at surfaces and interfaces) which may significantly alter defect populations and fluxes. The manner in which these additional defects will impact corrosion kinetics is comparatively very poorly understood, and it is far from clear that any of the trends that describe oxidation in conventional environments will still apply. In particular, non-equilibrium defects with low thermal populations that are created by irradiation might provide transport mechanisms not available by thermal self-diffusion.

*Corresponding author

Within the existing fleet of light water reactors, stainless steel has widely shown increased pitting and crevice corrosion in addition to substantially higher susceptibility to stress corrosion cracking compared to similar conditions without irradiation. Both effects are presently understood as consequences of electrolysis in the coolant water and/or microstructural and microchemical changes in the base metal, rather than differences in mass transport through the oxide itself[12, 13, 14, 15, 16, 17]. On the other hand, in the context of zirconium - used nearly universally for fuel cladding in existing reactors - recent models accounting for radiation enhanced diffusion (RED) in zirconia scales reproduced a pronounced acceleration in corrosion in high dose rate tests, but demonstrated minimal radiation effects in the lower damage rate PWR regime[18, 19]. Further, structural materials for next generation reactors will be exposed to different coolants, with a diverse set of possibilities including high temperature gas and lead-bismuth eutectic liquid metal, each of which have unique corrosion behavior[20]. For many fusion and advanced fission reactor applications, ferritic/martensitic steels with chromium content at or near 10 % are leading candidates to mitigate concerns with activation, void swelling, dimensional instability, and other effects unique to radiation environments[21, 22, 23]. These steels tend to form an inner layer of iron-chrome spinel beneath an outer layer of Fe rich oxide consisting of porous magnetite (Fe_3O_4) which may be decorated or capped with hematite depending on oxidizing conditions[24, 25, 26, 27, 28]. Provided a hematite scale is present and continuous, it is rate controlling for oxidizing pure Fe or Wüstite (FeO_{1-x})[29]. If absent, the Cr rich inner spinel layer becomes most protective.

In the case of hematite, tracer diffusion measurements at high temperatures have broadly shown similar transport kinetics on anion and cation sublattices[29, 30, 31, 32, 33]. Diffusivity broadly declines with oxygen activity, implying that anion vacancies and cation interstitials dominate mass transport, consistent with the iron rich deviations from stoichiometry in hematite[34]. However, it is far from clear that this will remain the case in an irradiation environment due to direct production of thermodynamically unfavored defects by ballistic recoil during radiation. Further, point defects in oxides may acquire different charge states - each with unique properties - and these charge states may change under irradiation. The preferred charge state depends on the location of the Fermi level within the band gap, which can change significantly due to disorder or off-stoichiometry induced by irradiation[35, 36, 37]. It stands to reason then that changes in the content of defects which mediate mass transport – whether due to oxide chemistry or exposure environment – can lead to a divergence in corrosion behavior from empirically calibrated models. Such a possibility motivates the development of theories which can account for and predict charge state transitions, and their impact on corrosion.

This work formulates a kinetic model for point defect transport that allows for the dynamic evolution of defect and charge density in a reaction-advection-diffusion framework. This proposed model encompasses processes such as interstitial-vacancy recombination, direct production in radiation events, development of space charge, and defect charge state transitions as the system evolves. First, we write the equilibrium conditions which determine thermal point defect content in kinetic rather than static form. A model built on this framework has the advantage of applying far from equilibrium, accommodating spatially dependent solutions, charge flow, and dynamic response to changing conditions. Next, we illustrate how this model can be directly tied to electronic structure calculations of key point defect properties and applied to hematite where a comprehensive library of these properties is well-known. Comparisons are drawn between the model and observed properties such as tracer diffusion and growth kinetics, showing good fidelity across a variety of exposure environments and temperatures. Finally, the model is used to predict changes in defect content and mass flow for both bulk hematite and protective hematite scales on materials exposed to radiation conditions typical of nuclear reactor and accelerated testing environments.

2. Methods

The objective of this model is to dynamically and self-consistently evolve point defect populations through the thickness of oxide films consistent with the chemical environment, any electric fields, and possible direct production from energetic particle collisions in a radiation environment. The manner in which these excess defects might modify mass transport through an oxide scale is illustrated schematically in Figure 1. To this end, we seek a kinetic formulation of the interaction of point defects with one another while allowing exchange of charges, and transport of both mass and charge. First, we describe the general framework for evolving species density beginning with the interactions between atomic defects, followed by a similar treatment for charge carriers and charged defects. The kinetic approach then extends to mass and charge transport, fully consistent with an evolving electrical potential. The model description concludes by showing how to define the model parameters from density functional theory (DFT) calculations for a particular material system.

In the cluster dynamics formalism[38, 39, 40, 41, 3, 42], the concentration c of each defect species i is governed by a diffusion-advection-reaction equation of the form

$$\frac{\partial c_i}{\partial t} = -\nabla \cdot \boldsymbol{J}_i + g_i - D_i k_i^2 \left(c_i - c_i^{th}\right) + R_i \tag{1}$$

where $\boldsymbol{J}$ is the flux, g is the rate of direct production in radiation events, D is the species diffusivity, k^2 is known as the sink strength, c^{th} is the thermal equilibrium concentration and R is the net rate of production or consumption in reactions. Flux is in turn determined by the chemical potential μ as

$$\boldsymbol{J_i} = -\frac{D_i c_i}{k_b T} \nabla \mu_i \tag{2}$$

where k_b is Boltzmann's constant and T is the temperature, which for the purpose of this model will be assumed constant. This section describes the formulation of each of the other terms in greater detail, particularly the reaction network R. This methodology is typically applied to simulate agglomeration of

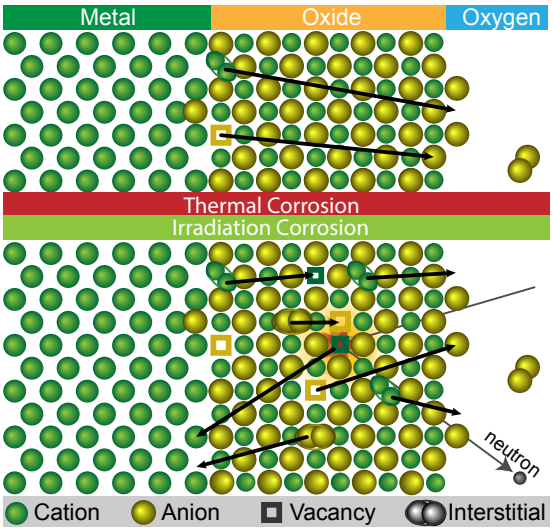

Figure 1: Comparison of oxide growth mechanisms in thermal and irradiation corrosion environments. In the thermal case, thermodynamically faroverd point defects form at one interface or the other and traverse the scale. Under irradiation, ballistic recoils produce mass-conservative pairs of point defects throughout the bulk, many of which would not be available from thermally activated processes.

radiation induced defects into large microstructural damage. In this application, it will be extended to included charge carriers, allowing charge state transitions to be represented as defect-carrier reactions[43].

2.1. Point defect chemical potential

For point defects in solids, the dilute limit is typically respected for any environment where the crystalline lattice remains stable, such that

$$\mu_i = H_i^f - TS_i^f + k_bT \log\left(c_i/c_i^0\right) + q_i\phi \tag{3}$$

where H^f and S^f are the enthalpy and entropy (excluding the configurational component) associated with forming the defect, c^0 the (sub)lattice site density, q the defect charge, ϕ the electrostatic potential, and the logarithmic term is the dilute limit configurational entropy. The formation energetics can be determined from atomistic calculations, but are inherently tied to a specific set of reference conditions. Here, the reference potential for oxygen will be O_2 at standard temperature and pressure, and the reference for electrons will be the middle of the undefected oxide band gap. In principle any reference can be taken, but must be consistent across all defect types considered.

When point defects form in the oxide by a charge conserving reaction with another phase (e.g. metal, oxygen gas, water, etc, the thermal equilibrium defect concentration near the interface is given by

$$c_i^{th} = c_i^0 \exp\frac{S_i^f}{k} \exp\frac{-H_i^f - \sum_i n_i^x \Delta\mu^x}{k_bT} \tag{4}$$

where $\Delta\mu^x$ refers to the difference in chemical potential for particle x (e.g. Fe, O, e^-, etc.) from the reference state defining H^f, and n_i^x is the change in the number of particles of x in the crystal by forming the defect (i.e. -1 for vacancies and +1 for interstitials). Note that for all charge conserving reactions, any dependence on ϕ must vanish, as in Eq (4). It will be convenient to define a free energy of formation

$$G^f = H^f - TS^f - n^x\Delta\mu^x \tag{5}$$

which accounts for all contributions to the thermodynamics except configurational entropy. As a concrete example, the charge neutral anion interstitial forming against oxygen gas follows

$$\begin{aligned} O_i^x &\leftrightharpoons \frac{1}{2}O_2 \\ H^f - TS^f + k_bT\log\left(c^{th}/c_O^0\right) &= \frac{1}{2}G_{O_2}(T,p) \end{aligned} \tag{6}$$

at equilibrium, such that $\Delta\mu^O = \frac{1}{2}G_{O_2}(T,p)$. Configurational entropy in the dilute limit is described by the logarithmic term, and leads to the definition of the equilibrium density specified by Eq (4). Importantly, for charged defects the electron chemical potential $\Delta\mu^e$ appears in G^f, a matter which will be treated in more detail later.

2.2. Kinetics of binary reactions

Point defects can react with one another, leading to either recombination or clustering into larger defect complexes. These processes take the form $A + B \leftrightharpoons C$. For example, recombination on the anion lattice follows $V_O^{q1} + O_I^{q2} \leftrightharpoons -(q_1+q_2)e^-$ where q_1 and q_2 are the charges on the vacancy and interstitial defects. When the energetics for the forward reaction are favorable and there is no short-range repulsion, the process is diffusion limited, and this is almost always the case for point defect interactions. For isotropic diffusion, binary reactions follow the Smolukowski rate[44, 45]

$$\dot{c}_A = \dot{c}_B = -\dot{c}_C = -4\pi r_{AB}\left(D_A + D_B\right)c_Ac_B \tag{7}$$

which defines the forward rate coefficient

$$k_{AB}^+ = 4\pi r_{AB}\left(D_A + D_B\right). \tag{8}$$

The reverse reaction is governed by a dissociation coefficient k_{AB}^-. When A, B, and C are in thermal equilibrium, both

$$k_{AB}^- c_C = k_{AB}^+ c_A c_B \tag{9}$$

$$\mu_C = \mu_A + \mu_B \tag{10}$$

must be satisfied, which is sufficient to determine

$$k_{AB}^- = k_{AB}^+ \frac{c_A^0 c_B^0}{c_C^0} \exp\frac{G_C^f - G_A^f - G_B^f}{k_bT} \tag{11}$$

where the numerator of the exponential defines the binding free energy between A and B. For recombination reactions, this is the Frenkel pair formation energy.

These equations are general for binary reactions, and used to construct all the reaction kinetics which factor into defect production and consumption R in Eq (1). Particularly, for a given defect i,

$$R_i = \sum_{j+k\to i}\left(k^+_{j,k}c_jc_k - k^-_{j,k}c_i\right) - \sum_{i+j\to k}\left(k^+_{i,j}c_ic_j - k^-_{i,j}c_k\right) \quad (12)$$

summed over all possible binary reactions that produce or consume species i. In this application, recombination between vacancy and interstitial type defects on the same sub-lattice are the predominant reaction, though the same equations apply to agglomeration of defects into larger clusters. In the case of pure recombination (where the defects are oppositely charged) there is no product species, such that the reverse reaction (Frenkel pair formation) rate becomes constant and c^0_C and G^f_C vanish from Eq (11). This fully describes reaction kinetics between point defects. We will now generalize to the case of charge transitions.

2.3. Delocalized electrons

The self-interstitial and vacancy defects on the atomic lattice are in some sense analogous to electrons and holes within the electronic system, though the physics governing the two systems is entirely different. The relationship between concentration and chemical potential is governed instead by Fermi-Dirac statistics, and takes the form

$$c_n = \int_{CBM}^{\infty}\rho(E)\left[1+\exp\frac{E-\mu_e}{k_bT}\right]^{-1}\mathrm{d}E \quad (13)$$

$$c_p = \int_{-\infty}^{VBM}\rho(E)\left[1+\exp\frac{\mu_e-E}{k_bT}\right]^{-1}\mathrm{d}E \quad (14)$$

for electrons (n) and holes (p) respectively. Here, μ_e is the Fermi level, $\rho(E)$ is the density of states (DOS) surrounding the band gap, and CBM and VBM are the conduction and valence band edges. When assuming that the DOS is well represented as a Fermi gas and that the Fermi level is at least a few k_bT away from the band edges, this reduces to

$$c_n = \left[2\left(\frac{m^*_nk_bT}{2\pi\hbar^2}\right)^{3/2}\exp\frac{-E_g}{2k_bT}\right]\exp\frac{\mu_e-E_{mg}}{k_bT} \quad (15)$$

$$c_p = \left[2\left(\frac{m^*_pk_bT}{2\pi\hbar^2}\right)^{3/2}\exp\frac{-E_g}{2k_bT}\right]\exp\frac{E_{mg}-\mu_e}{k_bT} \quad (16)$$

where $E_g = CBM - VBM$ is the band gap and $E_{mg} = VBM + E_g/2$ is the mid gap energy. Here, m^* is the effective mass of the electrons and holes, and encapsulates deviations of the actual DOS from the Fermi gas approximation. The terms in the square brackets are material properties with units of density, and are constant under isothermal conditions. These terms constitute c^0_n and c^0_p. Defining the reference potential for electrons as a system with the Fermi level at mid gap and $\phi = 0$ will prove convenient, as the electron and hole chemical potentials become

$$\mu_n = \mu_e - E_{mg} - \phi = k_bT\log c_n/c^0_n - \phi \quad (17)$$

$$\mu_p = E_{mg} - \mu_e + \phi = k_bT\log c_p/c^0_p + \phi \quad (18)$$

which can be viewed as distinct quasi-Fermi levels for electrons and holes.

The chemical potentials for charge carriers and point defects have the same functional form. Therefore, Eq (11) determines the constraints for charge carrier reactions between one another (electron-hole recombination) and with point defects (charge state transitions). The former is outlined below, while the latter will be examined in Section 2.4. Recombination follows $n + p \leftrightharpoons \{\}$, such that at equilibrium

$$k^-_{np} = k^+_{np}c_nc_p \quad (19)$$

$$\mu_n + \mu_p = 0 \quad (20)$$

which results in the law of electronic mass action,

$$c_nc_p = \frac{k^-_{np}}{k^+_{np}} = 4\left(\frac{k_bT\sqrt{m^*_pm^*_n}}{2\pi\hbar^2}\right)^3\exp\frac{-E_g}{k_bT}. \quad (21)$$

This reaction pathway constrains the density of electrons and holes in the system. Any deviation from Eq (21) which develops within the system will be remediated, either by pair production or recombination. The relaxation time for electronic equilibration is governed by the recombination constant. In principle, the kinetics of this process and the charge state transitions discussed next could be described with high fidelity quantification of the cross sections for recombination and carrier capture[46, 47]. For the purposes of the present application - which emphasizes ionic transport - it will be sufficient to apply Eq (8) with diffusivities for charge carriers much higher than those in the atomic system, effectively driving the system toward the Born-Oppenheimer approximation.

2.4. Charge state transitions

This model evolves electron and hole densities explicitly using the master equation - Eq (1) - while treating charge state transitions for point defects as binary reactions between defects and carriers. There are two principal advantages of solving the problem in this manner instead of using Fermi level dependent charge states and defect formation energies. First, it casts all charge state transitions as charge conservative binary reactions, meaning all kinetic coefficients become constants applicable across the entire band gap and independent of the electrostatic potential. Second, it allows the inclusion of a mixture of charge states simultaneously. In what follows, we will demonstrate these points using the example reaction $V^{\bullet\bullet}_O + n \leftrightharpoons V^{\bullet}_O$ (written using Kroger-Vink notation), with the equilibrium condition $\mu(V^{\bullet\bullet}_O) + \mu(e^-) = \mu(V^{\bullet}_O)$.

With no explicit reference to the electron as a reactant, this takes the form $V^{\bullet\bullet}_O \leftrightharpoons V^{\bullet}_O$ with

$$\dot{c}_{V^{\bullet\bullet}_o} = -\dot{c}_{V^{\bullet}_o} = \alpha_{V^{\bullet}_o}c_{V^{\bullet}_o} - \beta_{V^{\bullet\bullet}_o}c_{V^{\bullet\bullet}_o} \quad (22)$$

where α and β represent rate coefficients for electron absorption and emission from the vacancy, and will differ between charge states. In order to reach equilibrium one must write

$$\frac{\beta_{V^{\bullet\bullet}_o}}{\alpha_{V^{\bullet}_o}} = \exp\frac{1}{k_bT}\left[G^f_{V^{\bullet}_o} - G^f_{V^{\bullet\bullet}_o} - \mu_e - \phi\right] \quad (23)$$

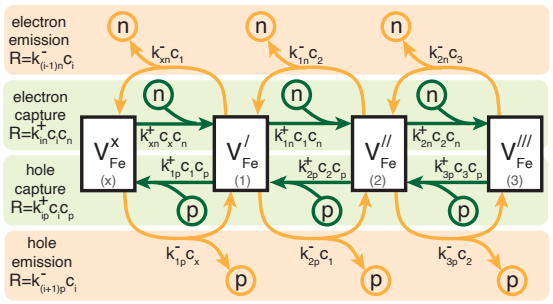

Figure 2: Recasting the charge state transitions into a kinetic reaction network which allows absorption and emission of charge carriers, and can facilitate an mixture of charge states, illustrated for the cation vacancy. Reaction rate coefficients are defined by constrained equilibrium conditions. Compressed notation is used for rate coefficient subscripts.

such that the forward coefficient, reverse coefficient, or both would need to be defined as variables dependent on the Fermi level and potential [1] , which in turn depend on $c(V_O^{\bullet})$ and $c(V_O^{\bullet\bullet})$. Every change in Fermi level will result in an evolving ratio of reaction coefficients, and therefore a change in the ratio between point defects at different charge states. This feedback loop between rate coefficients and defect density produces a poorly conditioned system that is difficult to solve as the complexity of the reaction network R increases.

In the approach used here instead, the electron density is evolved explicitly. In this case, one can use Eq (17) to expand the mass action relationship to

$$\dot{c}_{V_O^{\bullet\bullet}} = \dot{c}_n = -\dot{c}_{V_O^{\bullet}} = k^-_{V_O,n} c_{V_O^{\bullet}} - k^+_{V_O,n} c_n c_{V_O^{\bullet\bullet}} \tag{24}$$

$$\frac{k^-_{V_O^{\bullet},n}}{k^+_{V_O^{\bullet\bullet},n}} = c_n^0 \exp \frac{1}{k_b T}\left[G^f_{V_O^{\bullet}}\left(E_{mg}\right) - G^f_{V_O^{\bullet\bullet}}\left(E_{mg}\right)\right] \tag{25}$$

where the reaction coefficients are now constants determined solely by the formation energies of the defects. The appropriate reference level for defining the defect energies becomes at mid gap, and any dependence on electrostatic potential unambiguously vanishes from the energetics. This extends to other charge states for the vacancy, and may also include a similar set of reactions with holes, creating the reaction network illustrated in Figure 2 for vacancy charge state transitions. These evolve dynamically as new vacancies are introduced, until the electrons, holes, and vacancy charge states reach equilibration. Similar reaction networks can be established for other point defects, and are all coupled through the (dynamically evolving) electron and hole densities.

This reaction network is easily generalized to a wide set of interactions and charge state transitions and also more tractable from the standpoint of numerical integration than attempting to solve for the Fermi level directly. The densities of electrons and holes can simply be co-evolved with the densities of differently charged defects during dynamic simulation. As electron density c_n increases (implying a rising Fermi level) the forward reaction rate increases and the point defects favor a more negative charge state, and the opposite occurs should c_n fall. In this case, the reference formation energies for charged defects become well-defined constants - the mid-gap energies (where the reference concentration for μ_n and μ_p is defined). A similar absorption/emission balance is included for holes. In this way, maintaining a balance of charge states consistent with the electron potential is handled through the reaction network. Any pair of reactions out of equilibrium is driven toward equilibrium, and this proceeds dynamically as the populations of point defects evolve.

2.5. Polarons and Impurities

The same framework used here to describe the localization of charge carriers to point defects can also be applied to impurity elements (dopants) and primary constituent elements within the lattice (polarons). For impurity cations, the preferred ionization state of the impurities may be different than that of the host lattice. Using D to denote a dopant and Q to refer to the ionization state of cations in the pure material, one has the binary reactions $D^Q + e^- \leftrightharpoons D^{Q-1}$ and $D^Q + p^+ \leftrightharpoons D^{Q+1}$ for changing charge states. As with defects, these can extend to further charge states via additional reaction steps. The kinetics are governed by

$$\frac{k^-_{n,D^q}}{k^+_{n,D^q}} = c_n^0 \exp \frac{1}{k_b T}\left[G^f_{D^{q-1}}\left(E_{mg}\right) - G^f_{D^q}\left(E_{mg}\right)\right] \tag{26}$$

$$\frac{k^-_{p,D^q}}{k^+_{p,D^q}} = c_p^0 \exp \frac{1}{k_b T}\left[G^f_{D^{q+1}}\left(E_{mg}\right) - G^f_{D^q}\left(E_{mg}\right)\right] \tag{27}$$

such that the kinetic coefficients are determined by the change in system energy at mid gap as the impurity changes charge state. For a given charge state

$$R_{D^q} = k^+_{D^{q+1},n} c_{D^{q+1}} c_n + k^+_{D^{q-1},p} c_{D^{q-1}} c_p - \left(k^-_{D^{q+1},n} + k^-_{D^{q-1},p}\right) c_{D^q} \tag{28}$$

defines the net reaction rate.

For hematite in particular, the electron polaron strongly influences the behavior of the material. Intuitively, this follows from the flexibility of Fe to adopt Fe^{2+} and Fe^{3+} charge states, such that the reaction $Fe^x_{Fe} + n' \rightarrow Fe'_{Fe}$ has a (charge transition level) CTL deep below the conduction band edge. This has been found in DFT calculations [48, 49] and confirmed experimentally [50]. The hole polaron level is more controversial, with many calculations unable to localize the hole, others finding localization on O atoms using hybrid exchange-correlation functionals[51], and some experiments reporting Fe^{4+}[52].

Conductivity with polarons can occur either by delocalizing the charge or by direct transfer to a neighboring site. The former is accommodated directly by the reaction network (via the dissociation rates), while the latter implies a polaron diffusivity, governed by the reorganization energy for the localized charge to hop from one atom to the next[53, 54]. In this sense, polaron transport is analogous to lattice point defect transport. However, it is mathematically more complicated to implement, requiring an exchange current with neutral atoms in order to preserve lattice density. For this reason, only the delocalization

[1] The appearance of ϕ in this construction is ambiguous, and will depend on whether the Fermi level is referenced to the band edges or the vacuum level

process is included in this study. This simplification may impact electrical conductivity, but is not expected to significantly modify steady state space charge distributions or ionic transport of primary interest to the present study. Polaron reactions with mobile carriers (recombination) and mobile point defects (charge state transitions), however, are included.

2.6. Transport and boundary conditions

The flux of each defect and carrier follows from Eq (2). For all species, inserting the definition of chemical potential gives

$$\boldsymbol{J}_i = -D_i \left[\nabla c_i + \frac{q_i c_i}{k_b T} \nabla \phi \right] \tag{29}$$

and allows Eq (1) to be evolved solely in terms of species concentrations provided the electrostatic potential is known. This expression gives an accurate description of transport by both Fickean diffusion and electrostatically driven migration so long as $q\nabla\phi b << k_b T$ with b as the nearest neighbor spacing, typically valid outside the Cabrerra-Mott regime (films thinner than 10 nm). This study applies finite volume discretization[55, 56] for straightforward and exact enforcement of conservation principles for mass and charge flow. Simulations proceed by evolving the concentration of each defect species and charge carrier in time according to Eq (1) and concurrently updating the electrostatic potential according to any resultant space charge accumulation. For all species, spatial transport uses diffusion coefficients consistent with the construction of the reaction networks. Electron and hole mobilities are treated phenomenologically, but in principle could be described in greater detail to target electrical properties such as conductivity which are not critical in the current study.

For point defects, diffusivity will be defined here in terms of the usual Arrhenius relationship

$$D_i = D_i^0 \exp \frac{-E_i^m}{k_b T} \tag{30}$$

where E_i^m is the height of the saddle point along the migration pathway for species i to move from one lattice site to another. In non-cubic crystals (such as hematite), D may be anisotropic, a consideration beyond the scope of this study. The prefactor D^0 accounts for the attempt frequency, saddle point vibrational entropy, and jump distance, and is usually within the range 10^{-4} to 10^{-8} m^2/s.

All reactions defined in this framework are charge conservative, so only spatial transport of charged species can produce net space charge. When this occurs the resulting potential ϕ must satisfy Poisson's equation

$$-\epsilon \nabla^2 \phi = \sum_i (q_i c_i) \tag{31}$$

where ϵ is the permittivity of the material and the right hand side represents the net free charge density. At each timestep, the potential must be solved concurrently and consistently with reactions and transport. As described previously, the potential does not modify the structure or coefficients within the reaction network. Instead, it only modifies the spatial distribution of species through changes to the fluxes. As we show in Appendix A, the zeroth moment of the space charge distribution determines the net charge which must develop external to the scale to terminate any fields. Similarly, the first moment governs the voltage drop across the scale from the internal charge distribution. An additional uniform field may also be imposed across the scale based on external charge separation, and this can be reflected in the boundary conditions applied to the potential, and to the charge carrier concentrations.

The final term in Eq (1) is generation rates of radiation induced defects. This will take the form

$$g_i = c_i^0 \eta_i \Phi \tag{32}$$

where Φ is the mean displacement rate, usually given in displacements per atom per second (dpa/s). Many displaced atoms are eliminated rapidly through correlated recombination[57], and the displacement rate can vary between sublatticies with significantly different atomic mass. These effects are encapsulated in the parameter η, which can vary between conditions and here we use a uniform value of 0.1 for both O and Fe defects, though in practice it is likely to be for cation defects than anion defects. Radiation also creates electron hole pairs, and the number of such ionization events per displacement is a strong function of irradiation conditions.

We consider two options for charge flow at the boundaries: (a) insulating and (b) fixed potential conditions. The former follows Mott's concept of the oxidation process in dry air, shown schematically in Figure 3. Here, neutral oxygen atoms in the gas require electrons to become charged adsorbed anions, creating holes in the valence band and pulling the valence band maximum toward these adsorption states at the interface. If O_2 is not already ionized, this process must be charge neutral and the boundary is insulating. In contact with a metal on the other hand, electrons can be transferred to and from the metal, such that the Fermi level at the interface is pinned to the Schottkey barrier for inserting electrons into the oxide. Both conditions allow for space charge accumulation and a net potential drop across the film. For thick oxide scales, most of the material sits at the charge neutrality level.

For a purely insulating boundary the net charge carried across the interface must be zero. Imposing a zero flux boundary condition on all charged species at the interface is the simplest means to satisfy this condition. The density of neutral species (e.g. point defects) at the interface follows Eq (3), defined by local equilibrium with the adjacent phase. This constraint is sensitive to Fermi level and electrostatic potential for charged species, but fully independent of these quantities for neutral ones. Thus, the neutral defect concentrations at an interface are determined only by the chemical activity (e.g. $\Delta\mu^O$) which are properties of the neighboring phase. Charged defects at an insulating interface form subsequently through the reaction network, consuming or producing electrons and holes to change charge state. That is, we do not consider the direct formation of charged species at the interface but rather allow them to evolve from the formation of neutral defects. The quasi-Fermi levels at an insulating interface float together with the densities

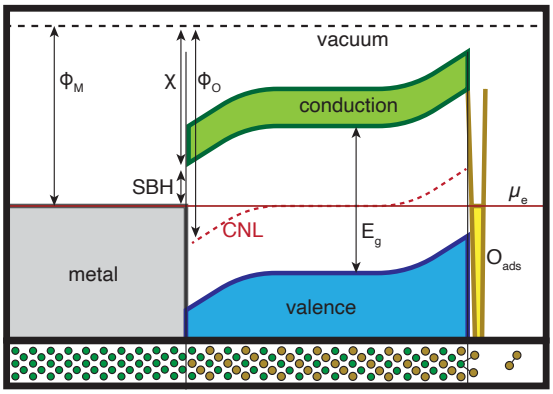

Figure 3: Example of electron energy levels within an oxide scale growing on metal in air. Band levels near the boundaries can be influenced by oxide termination conditions, with internal band bending governed by space charge density consistent with Eq (31). For sufficiently thick scales, the interior of the oxide away from the influence of adsorption states or the Schottkey barrier reverts to the charge neutrality level (CNL).

of charged defects toward a constrained equilibrium, reached within the relaxation time of the electronic system. Adsorption states can be included as a set of species which occupy only the interface integration point, and do not diffuse into the bulk crystal. For this work, the charge transition levels of the oxygen interstitial were replicated for adsorbed oxygen.

Conducting boundaries are simpler to enforce, and the net charge flux need not be zero. Instead, the electron and hole potentials are fixed (much the same way as the neutral defects) to maintain a prescribed Shottky barrier height (SBH) between the conduction band edge in the oxide and the electron potential in the conductor. This results in a well-defined Fermi level at the interface, allowing the density of all species at the interface to be determined *a priori*, not just neutral ones. This allows flexibility for the charged species (other than electrons and holes) to be handled either (a) through the reaction network, similar to the insulator or (b) by directly applying Eq (4) while including any change in Fermi level from mid gap in $\Delta\mu^e$. In practice, the SBH is often influenced by charge dipoles and the character of the interface such that "bulk" work functions (ϕ_M,ϕ_O) and electron affinities (χ) are poor descriptors of the SBH[58]. As such, the nature of this potential is interface dependent, and much more difficult to determine directly from *ab initio* calculations than point defect properties.

2.7. Parameterization

Formation energies of point defects can be found from atomistic simulations. Following the Zhang-Northrup formalism[59], the formation energy of defect X can be written

$$H_i^f = E[X_i] - E[0] + E_{\text{corr}} - \sum_j \mu_*^j \left(n^j[X] - n^j[0]\right) \quad (33)$$

where $E[X_i]$ is the energy of the cell with the defect i, $E[0]$ is the energy of the perfect cell, and E_{corr} is a correction which accounts for any (artificial) interaction of the defect with itself across periodic boundaries, typically due to charge or strain[60, 61, 62]. Finally, n_j is the number of particles of type j in the cell, and μ_*^j is the DFT chemical potential of those particles. This is subject to the constraint $E[0] = \sum_j n^j \mu_*^j$, such that a system with N elements leaves $N-1$ degrees of freedom in choosing reference chemical potentials.

This work aligns the reference for oxygen to oxygen gas at STP. This sets the reference potential at half of the energy of an O_2 molecule. However, it is well known that (a) many DFT appoaches overbind oxygen[63, 64], (b) those with a Hubbard U parameter often do a poor job of representing the heat of formation for transition metal oxides[65, 66] and (c) the STP reference for O_2 gas used in practice is neither at the same pressure (indeterminate) nor temperature (0K) as the DFT calculations[67]. A number of corrections have been proposed to try to accommodate some of these shortcomings[68, 69, 70]. Here, we include only a single offset energy ζ to account for all artifacts in chemical potential alignment at the DFT level

$$\begin{aligned} \mu_*^{\text{O}} &= \frac{1}{2}E[\text{O}_2] + \zeta \\ \mu_*^{\text{Fe}} &= \frac{1}{2}\left(E[\text{Fe}_2\text{O}_3] - 3\mu_*^{\text{O}}\right) \end{aligned} \quad (34)$$

which is treated as a fitting parameter. The change in chemical potential against this reference follows the formulae in Table 1 and tabulated thermochemistry data for hematite, O_2 (oxygen rich conditions), and magnetite (metal rich conditions)[71]. Migration energies are not influenced by chemical potential and can be found using saddle point identifying techniques such as nudged elastic band methods[72]. Point defect thermokinetics information for Fe_2O_3[73, 74, 75, 48] is summarized in Appendix B.

	O_2	Fe_3O_4
$\Delta\mu^{\text{O}}$	$G_{O_2}(T,p)$	$3G_{Fe_2O_3}(T) - 2G_{Fe_3O_4}(T)$
$\Delta\mu^{\text{Fe}}$	$\frac{1}{2}G_{Fe_2O_3}(T) - \frac{3}{2}G_{O_2}(T,p)$ $-\frac{1}{2}G^0_{Fe_2O_3}$	$3G_{Fe_3O_4}(T) - 4G_{Fe_2O_3}(T)$ $-\frac{1}{2}G^0_{Fe_2O_3}$

Table 1: Deviation in cation and anion potentials in hematite defined with respect to the STP O_2 reference state. Formulae are given for reactions with either oxygen gas or magnetite. $G_X(T,p)$ is the tabulated molar free energy of phase X, while G_X^0 is its value at STP.

Together, this fully parameterizes Eq (1) for evolving the defects in an oxide with spatial resolution. In this study, this capability will be used to simulate the concurrent transport of charged point defects through a film. Anion and cation defects of both interstitial and vacancy character are included, coupled through charge reactions with delocalized electrons and holes, as well as polarons. The resulting electrostatic potential and mass flux across that develops within oxide scales can be determined for conventional thermal corrosion in addition to irradiation affected environments.

3. Results

This section reports the behavior of the model as applied to hematite. First, we will demonstrate the ability of the model to reproduce the bulk properties of hematite at high temperature by benchmarking to experimental data and analytical expressions for well-equilibrated states. Next, we examine the kinetics of oxidation of magnetite (Fe_3O_4) to hematite in dry air, which compares favorably to experimental reference measurements. This is followed by a transition to the effects of irradiation, looking first at changes in the defect populations and Fermi level in bulk material. Finally, we look at changes in the oxidation kinetics under irradiation, often finding a counter-intuitive reduction in corrosion kinetics in irradiation environments, though the effect is non-monotonic in nature. By activating individual mechanisms separately, the origin of this effect is identified as an internal potential from charged vacancies which inhibits cation flux, and can induce transitions in charge state for the cation interstitial from $Fe_I^{\bullet\bullet}$ to the less mobile $Fe_I^{\bullet}$.

3.1. Pure hematite

Simulations of bulk hematite were carried out using 1d slabs of hematite material with interfaces on either side corresponding to oxygen gas as illustrated in Figure 4. The crystal was initialized in an undefected state, and promptly heated to a fixed temperature. After initialization, point defects flow in from either surface, evolving dynamically until reaching a well equilibrated condition. The mean charge of the defect species evolves consistently with the Fermi level until reaching an equilibrated state. Due to the insulating boundary conditions and conservative nature of the reaction network and integration scheme, the net system charge remains zero to within numerical precision throughout the simulations. Simulations of this type were repeated for a wide range of temperatures and oxygen activities.

Defect densities in the center of a hematite slab once steady state is achieved can be compared to the experimental properties on stoichiometry and mass transport in hematite. The self-diffusion and high temperature oxygen deficiency of hematite can be captured accurately both with and without inclusion

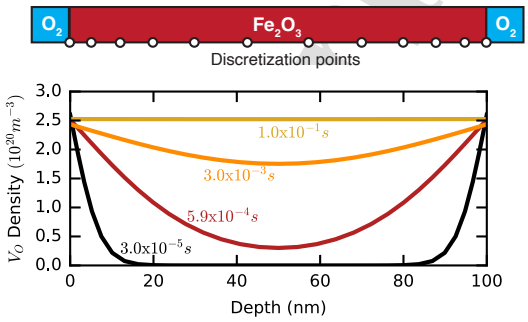

Figure 4: Basic cluster dynamic type simulations of charged defect profiles in hematite showing an illustration of a 1d simulation of a hematite film in air and the evolution of anion vacancy profiles upon prompt heating to 800 ^{0}C.

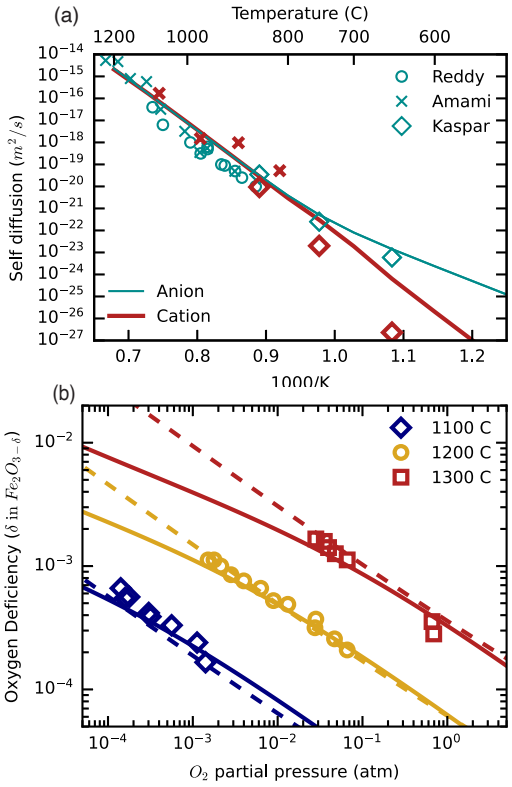

Figure 5: Comparison of the performance of the kinetic model (lines) to the empirically observed (points) high temperature behavior of hematite(points). The (a) self-diffusion from the model including polarons for hematite exposed to air is compared to both anion and cation measurements with conventional tracer diffusion experiments from Amami et al[31] and Reddy et al[30] and atom probe enabled measurements from Kaspar and co-workers[76]. The oxygen deficiency (b) is compared to the data reported by Dieckmann[34], for both the polaron (solid lines) and polaron-free models (dashed lines).

of the polaron state, as shown in Figure 5. With polarons omitted, oxygen deficiency declines strictly to the power 1/2 with O_2 partial pressure, consistent with neutral anion vacancies. When polarons are included, the power law exponent of pressure dependence varies, and this occurs due to a transition from charged to charge neutral vacancies as oxygen activity increases. Self-diffusion on both lattices compares well to the experimental measurements, and thermal self-diffusion measurements are included from both conventional tracer diffusion measurements, and more recent work at lower temperatures enabled by atom probe tomography characterization across finer length scales. An apparent change in activation occurs in the anion self-diffusion, and reflects a transition from vacancy meditated to interstitialcy mediated transport as temperature decreases. This possibility was suggested in prior work which did not allow for changes in Fermi level[77], and it remains active

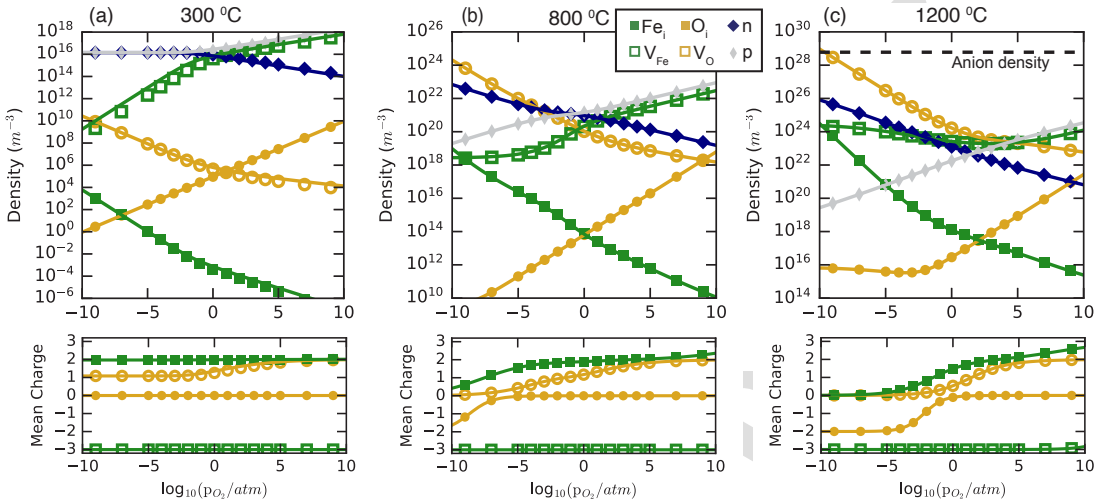

Figure 6: Brouwer diagrams of the defect content in hematite at (a) 300 (b) 800 and (c) 1200 ^{o}C when polaron states are omitted. In each case, the upper panel shows net defect density summed over all charge states while the lower shows mean charge for each point defect class. Points are determined by the equilibrated state of a hematite slab using the kinetic model proposed for this work, while solid lines are computed by finding the charge neutrality level according to Eq (36)

in the full model here.

In bulk material, equilibrium defect content respects a self-consistent solution to the charge neutrality condition

$$0 = \sum_j q_j c_j. \tag{35}$$

So long as the dilute limit is respected and the Fermi level does not encroach on either band edge, the concentrations are determined as

$$c_j = c_j^0 \exp \frac{E_j^f(T,p) - q_j\left(E_F - E_{mg}\right)}{k_b T} \tag{36}$$

for each species j. The resulting sum is transcendental in Fermi level, but can be solved by fixed point iteration to determine the charge neutrality level (CNL) corresponding defect and carrier densities[78] that satisfy charge neutrality. The calculated CNL and defect densities from this approach are essentially identical to the equilibrium condition attained by the dynamic model in the center of a hematite slab once steady state is achieved, as shown for a wide range of oxygen pressures at selected temperatures in Figure 6 for a case where polaron states are neglected[2]. At 300^{0}C, the population of cation vacancies was still slowly increasing, and had not fully equilibrated at the simulation end time owing to the high migration barriers for these defects. This is appears as a slight difference between analytical equilibrium and simulated vacancy content.

As temperature increases, the intrinsic region (where $c_n \approx c_p$) narrows because the ratio of point defects to charge carriers increases and requires additional charge compensation. At high temperature, the material displays n-type behavior for oxygen pressures below atmosphere, consistent with the known properties of the mineral[34]. As the Fermi level continues to rise with decreasing O_2 pressure, the CTL to lower charge states is passed. The anion vacancy prefers +1 at mid gap, and the cation interstitial prefers +2, but both are pushed toward charge neutral states as oxygen activity drops. At lower pressures still, the anion interstitial transitions to the −2 charge state. The cation vacancy is already at its lowest charge state (−3) at mid gap, and remains there for every thermal condition simulated in this study. These charge transitions - evident in the lower panels of Figure 6 - are not step-wise binary process, and instead occur via a mixture of defect charge states with ratios that evolve with oxygen activity. This is reflected in a non-integer mean charge for each point defect type, one that increases smoothly with oxygen activity alongside a corresponding drop in Fermi level. The reaction network based approach captures this behavior inherently, dynamically, and - as will prove important in the subsequent results - in a manner that respects spatial gradients.

3.2. *Oxidation kinetics*

Mass transport through the hematite layer of an oxide scale was simulated by changing one of the boundaries to have an oxygen chemical potential consistent with magnetite. This can represent either the oxidation of bulk magnetite to hematite or the magnetite sublayer which forms in oxide scales during the corrosion of Fe metal. In either case, the lower oxygen potential at the inner (magnetite/hematite) boundary drives a net flux of oxygen inward and metal outward. Following an approach otherwise identical to the bulk material, defects flow in from the

[2]Similar agreement is attained when polaron states and/or dopant atoms are included, but these diagrams are omitted for brevity.

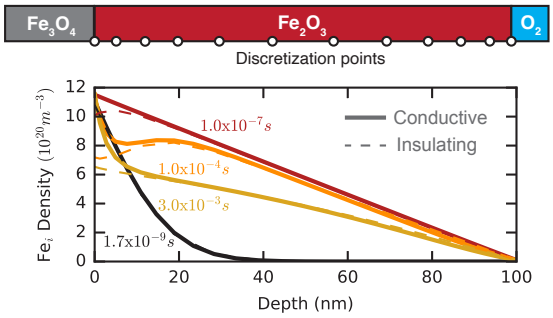

Figure 7: The evolution of cation interstitial profiles upon prompt heating to 800 ^{0}C in a 100 nm thick film of hematite grown on magnetite. Defect flux first increases, then decreases with time, with space charge accumulation occurring in the first 10 nm of the film. Changing the inter-oxide boundary condition from a fixed Fermi level (conductive) to zero charge flux (insulating) modifies only the boundary layer.

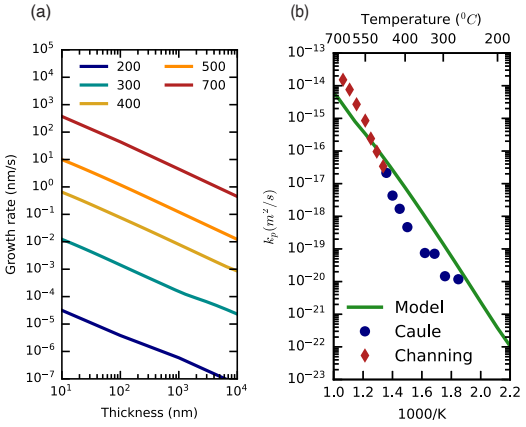

Figure 8: Oxide growth rates calculated from steady state defect flux shown (a) as a function of film thickness at selected temperatures and (b) using extracted parabolic rate constants and compared to experimental measurements of hematite growth from Caule[79] and Channing[80, 81].

boundaries and evolve until reaching steady state. The simulation setup and evolution of defects in a passive scale are shown in Figure 7.

Two limiting cases are shown commensurate with the previously discussed boundary conditions. In the first, magnetite is treated as a conductor, and the Schottkey barrier at the interface (electron potential) is held fixed midway to the polaron level. In this case, a significant positive space charge develops in the first 10 nm of the film, primarily from anion vacancies. A nearly linear cation defect profile is established within a 100 ns. As the slower anion vacancies diffuse in over several ms, space charge accumulates near the interface, causing a noticeable drop in $Fe_i^{\bullet\bullet}$ concentration and corresponding flux. This serves as a barrier for injecting these defects into the scale, and induces a drift current opposing the concentration gradient, slowing net cation transport. In the second, magnetite is treated as an insulator, and the flux of charge across the interface is zero. In this case the Fermi level at the interface rises, lowering the cation interstitial density directly at the interface, but space charges are much less pronounced. Outside of the first 10 nm, defect concentrations are almost identical, and the steady state flux is not substantially influenced.

In these simulations the boundaries are held fixed, such that the growth of the film cannot be simulated directly. In this case, the final product of the simulation is not an equilibrium condition, but rather a steady state flux of O and Fe atoms through a hematite scale of a given thickness. The corresponding growth velocity of hematite when this condition is reached follows

$$v = \Omega_{Fe_2O_3} (4.5 j_{Fe} - 3 j_O) \tag{37}$$

where $\Omega_{Fe_2O_3}$ is the formula unit volume. This follows from the 4 formula units produced for each Fe atom that leaves the magnetite interface, 3 for each O that arrives there, and half a formula unit for each Fe that reaches the oxidizing environment, consistent with the reactions

$$\begin{aligned} 3Fe_3O_4 &\rightarrow Fe + 4Fe_2O_3, \\ 2Fe_3O_4 + O &\rightarrow 3Fe_2O_3, \text{ and} \\ Fe + 3/2O_2 &\rightarrow 1/2Fe_2O_3. \end{aligned} \tag{38}$$

Bringing scales of different thickness to steady state determines the growth trajectory for scales in excess of about 10 nm, where the initial transient may influence kinetics. Growth rate as a function of thickness for hematite growing on magnetite is shown for selected temperatures in Figure 8.

The strictly inverse relationship between thickness and growth rate displayed by this model characterizes conventional diffusion-controlled parabolic oxidation. The parabolic rate coefficient (by thickness x) for this process can be written

$$k_p(T) = \dot{x}(T, x)/x \tag{39}$$

and quantifies the growth kinetics in a manner that can be compared to experimental data. Arrhenius plots of simulated and experimentally measured oxidation kinetics are also given in Figure 8. At all temperatures, growth was mediated solely by the outward flow of cation interstitials with all other defects providing negligible contributions to growth. The majority charge state was $Fe_i^{\bullet\bullet}$, with some triply and single charged defects present, particularly as temperature increased. The activation energy and magnitude of corrosion kinetics demonstrate reasonable agreement with experimental work. Caule et. al. quantified the hematite and magnetite layers separately, identifying an early time regime where magnetite thickness was constant and growth proceeded only by hematite expansion[79]. At higher temperatures, Channing and co-workers oxidized Fe films, measuring the later progression of hematite growth after all underlying metal had converted to magnetite[80, 81]. Both

cases isolate exactly the processes simulated here, and these data are also shown.

An analysis by Atkinson and Taylor[29] concluded that a notional parabolic constant for Fe oxidation accounting for the multi-layer scale structure of Fe/FeO/Fe_3O_4/Fe_2O_3 collapses oxidation rates for Fe metal, FeO, and Fe_3O_4 substrates onto a single curve. This provided an activation energy similar to self-diffusion by n-type defects in hematite generated at the hematite/magnetite interface. Their analysis implies mass transport through hematite is rate limiting during Fe oxidation, and occurs by Fe_i or V_O migration. Our model produces a similar agreement in activation energy for parabolic oxidation kinetics, and suggests $Fe_i^{\bullet\bullet}$ transport alone mediates hematite growth. Extrapolating from high temperature diffusivity data, the notional rate constant analysis of Aitkinson and Taylor underpredicted oxidation kinetics by 1-2 orders of magnitude. Our model, however, agrees for both activation energy and magnitude.

Another feature of the model is that the parabolic constants above 500 ^{0}C do not follow a strictly Arrhenius relationship, though the deviation is subtle. This is due to a rising density of $V_O^{\bullet\bullet}$ defects which begin to shift the Fermi level toward the conduction band. These defects outnumber Fe interstitials by several orders of magnitude, but owing to their low relative mobility make vanishing contributions to oxide growth. This results in an extra barrier for inserting $Fe_i^{\bullet\bullet}$ defects into the charge neutral region of the oxide per Figure 7, and an increasing fraction of $Fe_i^{\bullet}$ defects, which are less mobile than their doubly charged counterparts (see Appendix B). This subtle decrease in effective mobility at high temperature may well explain why the direct extrapolation by Atkinson et al from high temperature data gives lower expected rate constants than seen here. The activation energy in the linear regime does not perfectly match the experimental data, and linear regression indicates a 0.1 eV difference, well within the margins between different levels of theory for computing formation and migration energies in DFT.

3.3. Irradiation-induced defects

Irradiation produces defects throughout the material, rapidly generating a supersaturation of both vacancy and interstitial defects. For hematite in air, the evolution of defect content is opposite from the prompt heating shown earlier. Instead of flowing in from surfaces, vacancies accumulate in the interior and flow outward to the surface. Eventually, a steady state profile is reached, with more defects in the center of the material than at the surfaces as shown in Figure 9. Cation vacancies also accumulate in the material ultimately reaching a higher density due to lower mobility as compared to anion vacancies. Consequently, more of cation vacancies are annihilated by recombination rather than diffusion to surfaces. Further, cation defects are oppositely charged and attract while anion interstitials are charge neutral. This further increases recombination density for cation defects, as the electrostatic fields developed by the cation vacancies restricts the escape of interstitials to the free surfaces.

The significantly higher mobility of interstitial defects on both sublattices leaves far fewer present in the material, shown

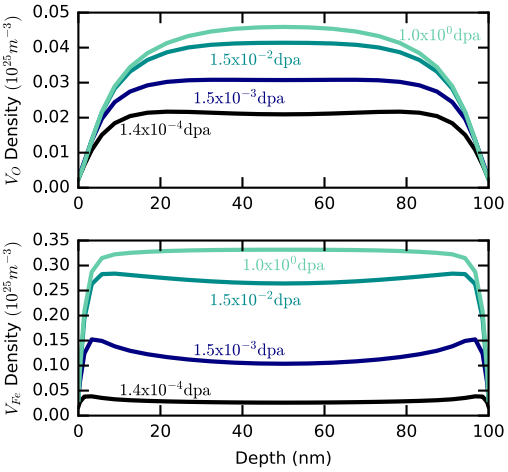

Figure 9: Depth distribution of anion and cation vacancy net density (summed over all charge states) in a thin film of hematite irradiated at 300 ^{0}C and 10^{-6} dpa/s, shown at selected doses.

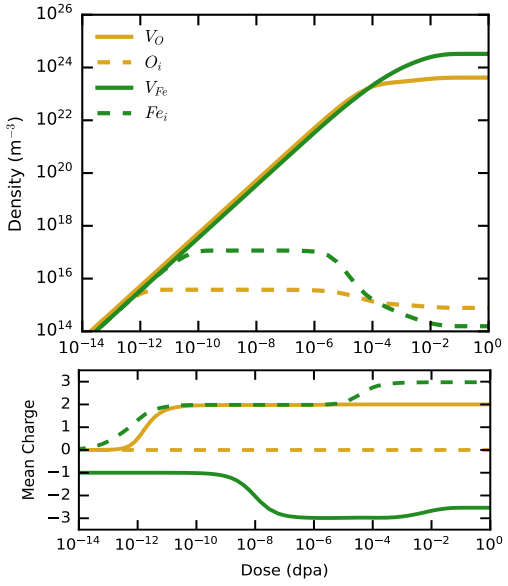

Figure 10: The evolution of total density and mean charge of interstitial and vacancy defects on both anion and cation sublattices with dose at 300 ^{0}C.

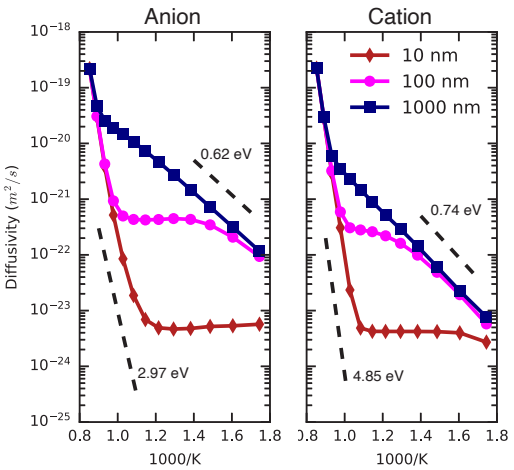

Figure 11: Self diffusion coefficients during irradiation at 10^{-6} dpa/s and three different film thicknesses shown separately for the cation and anion sublattices. The high temperature thermal diffusion regime and low temperature recombination dominant regime are evident, and the expected activation energies for each condition is indicated. An intermediate sink-dominant regime with no temperature dependence appears for thinner specimens.

in Figure 10. While the vacancy species linearly accumulate to at least a few dozen appm, interstitial densities saturate almost immediately at far lower concentrations. As vacancy densities continue to climb, interstitials begin annihilating by recombination before reaching surfaces, and their densities drop further. This is particularly true on the cation lattice, but evident to a lesser extent for anions as well. This general behavior of vacancy and interstitial defects is typical during irradiation[82]. Another consequence of the rising cation vacancy supersaturation is a falling Fermi level, reflected in the lower panel of Figure 10. These defects absorb electrons during the transient [3] because their preferred charge state is V'''_{Fe}. By 10^{-4} dpa, the Fermi level drops below the +2/+3 CTL for cation interstitials, and by 10^{-2} dpa stabilizes near the -3/-1 CTL for the now preponderant cation vacancy.

The additional defects present under irradiation lead to higher mobility of atoms and faster self-diffusion on both sublattices. The extent of this radiation enhanced diffusion (RED) depends on the mean free path of defects to annihilation, which is influenced by both microstructure and recombination density. Figure 11 shows the self-diffusion during irradiation for films with several thicknesses. At large thickness (low sink strength) diffusivity transitions between two Arrhenius regimes, high temperature thermal self diffusion and a low temperature regime governed by diffusion of irradiation induced defects, with densities limited primarily by recombination.

At higher sink densities (thinner films), there is a transitional region with no temperature dependence. In these conditions, recombination is negligible, and defect densities are limited purely by loss to sinks. As shown in Appendix C, the radiation enhanced diffusion coefficient in these cases becomes

$$D^{\mathrm{RED}} \approx \frac{2g}{c_0 k^2} \tag{40}$$

with equal contributions from vacancy and interstitial defects. As temperature continues to drop, the recombination regime is reached. Under these conditions, one instead finds

$$D^{\mathrm{RED}} \approx \frac{1}{c_0}\left(\frac{gD_v}{2\pi r_{iv}}\right)^{1/2} \tag{41}$$

with an effective activation energy of half of the vacancy migration barrier. These simple approximations describe the full simulation results well, though small deviations are evident from the influence of space charge accumulation on the defect content. This is most evident for anion diffusion in the 10 nm film, where a slight negative activation appears. Radiation induced space charges will play a much more significant role in transport through growing oxides, discussed at length in the next section. Finally, we note that in cases where both vacancy and interstitial defects become immobile, RED will occur primarily by ballistic mixing directly in damage events, rather than by transport of point defects. In hematite, both cation and anion interstitials are mobile even at room temperature and this regime is unlikely for any of the conditions considered here.

This compares well to the dose and temperature dependence of experimental measurements of RED in hematite in general[83]. However, the recombination limit for anions and cations seen in experiments was notably closer in magnitude than seen here. This likely reflects coupling of the two lattices through defect clustering into larger agglomerates of vacancy and/or interstitial defects. Regardless, the effects of irradiation significantly enhance atomic mobility within the oxide. As we show next however, this only translates into accelerated oxidation kinetics under very specific conditions. In fact, in many conditions oxide growth may actually be slowed.

3.4. Oxide growth during irradiation

This subsection outlines the influence of irradiation on the scale growth conditions outlined in section 3.2. First we demonstrate a somewhat counterintuitive reduction in oxidation kinetics during irradiation at technologically relevant temperatures. Isolating and selectively removing individual aspects of the physics from the model demonstrates that this effect stems from shifts in the charge neutrality level detrimental to cation interstitial transport. Other factors are also active, including drift flux in the electric field and internal recombination in the oxide scale, but less pronounced.

Irradiation generally suppresses oxidation kinetics in the fission reactor relevant regime of dose rates and temperatures, as seen in Figure 12. Data are shown for 10^{-9} dpa/s relevant to pressure vessels and spent fuel, 10^{-6} dpa/s as expected for fast reactor cladding, and 10^{-3} dpa/s typical of accelerated material testing in ion beam facilities. The effect is non-monotonic,

[3] Moving through the unstable V''_{Fe} state (which does not lie on the convex hull) slows the kinetics of reaching this charge in comparison to the cation interstitial and anion vacancy

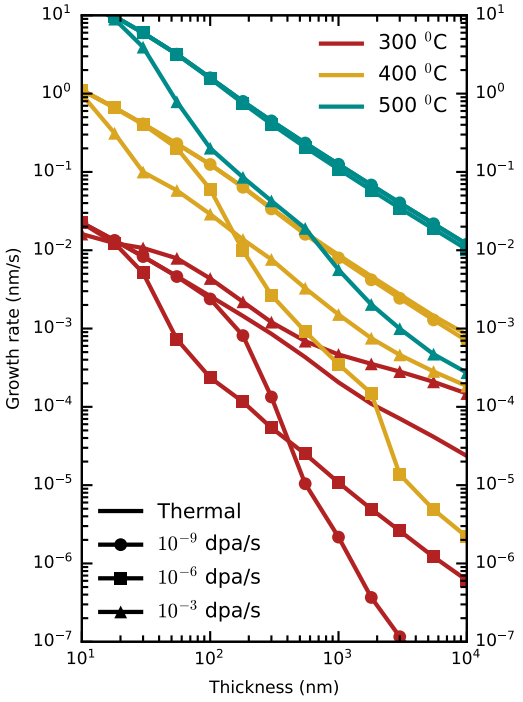

Figure 12: Hematite growth rates at a dose of 1 dpa as a function of oxide thickness during continuous irradiation. Selected dose rates are compared to thermal growth for three temperatures demonstrating a non-monotonic effect of increasing damage rates and deviations from parabolic growth.

and both 300 and 400^{0}C simulations show slowing growth with damage at low dose rates, which then transitions to a recovery or even increase in growth rate when reaching the highest dose rates. At the higher temperatures, radiation has no effect at sufficiently low damage rates, and growth becomes indistinguishable from the thermal case. The growth trajectory does not follow parabolic trends overall once radiation is introduced, though in many cases $\dot{L} \approx 1/L$ still holds for selected ranges of thickness. Interestingly, for the highest dose rate, the growth trends at all temperatures converge toward a single curve at large thickness.

Lack of a clear and uniform effect suggests multiple competing mechanisms are active. The absence of any effects at high temperature are relatively easily explained by the abundance of thermal defects overwhelming radiation induced defects in transport processes. The critical temperature for this to occur naturally increases with internal densities of radiation induced defects, and therefore with dose rate. Such effects have been widely observed in other aspects of irradiation damage[84]. The other mechanisms are more difficult to identify, but in what follows, we consider three possibilities: recombination altering the distance atoms need to travel, separation of oppositely charged defects by an electric field, and irradiation induced shifts in the Fermi level.

Removing all the electrostatic dependencies of the problem isolates the first mechanism. To accomplish this, all defects are made charge neutral, with formation and migration energetics fixed to the CNL energies. This simplified problem has only four species, no electrons or holes, and no space charge. In this case, the only effect of irradiation is to increase growth rates, as seen in Figure 13 at 300 ^{0}C and 1 dpa for several growth rates. However, the nature of this effect is transient, as demonstrated in 13(b). The apparent growth rates as a function of dose (time) show a radiation induced transient stage, many orders of magnitude longer than for thermal growth. The thermal transient for the conditions examined resolves within 1 ms, but under irradiation a second transient appears that persists for hours. Once steady state is reached, identical kinetics to thermal conditions are restored. Furthermore, suppressing recombination leads to a net flux which matches thermal conditions throughout the simulation (not shown) with no additional transient stage. Despite significant radiation enhanced diffusion, oxidation kinetics are identical.

This may seem counter-intuitive, but follows directly from point defect partitioning. Radiation induced defects are intrinsically mass conservative overall, so if half the interstitials arrive at each interface, and same for vacancies, it results in no excess mass flux. With only Fickean diffusion operating, the radiation induced populations superimpose linearly on the concentration profiles from the thermal defects, and only the thermal flux remains unchanged. Recombination between thermal and irradiation induced defects breaks the the linear superposition principle, but only during dynamic evolution in the transient stage before the vacancy content reaches steady state. While vacancies are still accumulating within the scale, mass conservation implies excess interstitial flux to the interfaces. Any excess mass arriving at phase boundaries is merely a consequence of an increasing vacancy population. It is difficult to sustain vacancy densities against recombination at higher than 1000 ppm, suggesting that the transient stage can account for no more than an 0.1% increase in oxide thickness in practice. Indeed, integrating the excess growth from the irradiation transient in Figure 13(b) gives less than 1 nm excess growth for a 1000 nm oxide.

Returning to the full problem with electrostatic effects and space charge, drift in an electric field can polarize the flux of oppositely charged interstitial and vacancy defects in opposite directions, breaking the symmetry of the pure diffusion problem. The excess vacancies accumulated in the scale do induce significant space charge. This leads to an internal potential and corresponding shift in the Fermi level, which remains present when steady state is reached. The strong preference for $V_{\mathrm{Fe}}^{\prime\prime\prime}$ pushes the electron level toward the valence band, while $V_{\mathrm{O}}^{\bullet\bullet}$ pushes it toward the conduction band. The latter effect is seen in the thermal case at high temperature, but under irradiation they compete. To demonstrate this competitive effect, simulations where one type of vacancy is restricted to the neutral state are shown in Figure 14. Simulations that enforce V_{O} neutrality result in falling Fermi levels, and accelerated corrosion.

Demanding V_{Fe} neutrality instead creates an opposite Fermi level shift, with magnitudes sufficient to induce a charge state

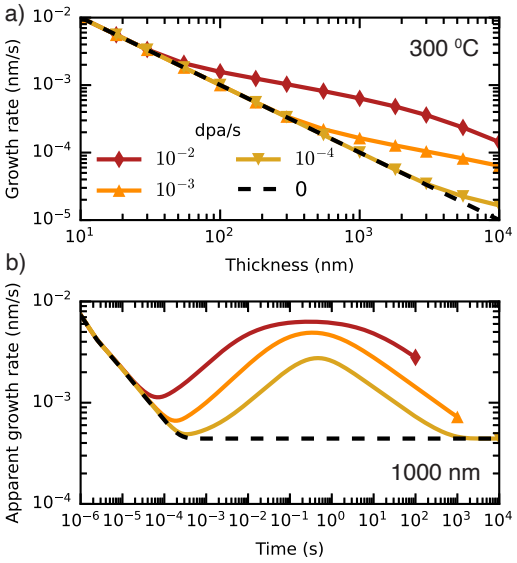

Figure 13: Growth rates when defect charge and charge state transitions are neglected. Thermal growth is compared to several irradiation dose rates (a) as a function of thickness at 1 dpa and (b) as a function of dose (up to 1 dpa) at a fixed thickness of 1 μm.

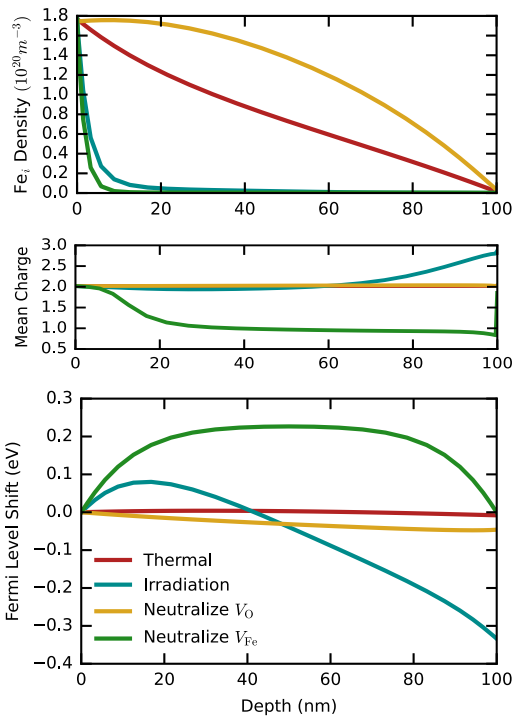

Figure 14: The density (top) and mean charge (center) of cation interstitial defects flowing through a hematite film growing on magnetite at 400 ^{0}C during irradiation at 10^{-3} dpa/s, along with the corresponding shift in the Fermi level as a function of depth(bottom). This data is shown for the DFT predicted properties of hematite alongside the irradiation free (thermal) reference case and cases where either anion or cation defects restricted to the charge neutral state.

transition to $Fe_i^{\bullet}$. This charge state has a significantly higher migration barrier than $Fe_i^{\bullet\bullet}$, further suppressing cation transport. The effects do not superimpose linearly when both vacancy supersaturations are free to transition between charge states. Near the magnetite layer, most V_{Fe} are recombined by thermal Fe_i leaving an n-type shift, and a barrier to further inward $Fe_i^{\bullet\bullet}$ fluxes. Consequently, near the outer surface a much higher density of V_{Fe} are left, and material shifts significantly p-type. The separation of charge induces a 300 mV potential drop across the scale, but a nearly 100 mV internal barrier height.

This n-type barrier is rate-limiting for cation transport, resulting in the decrease in corrosion kinetics seen for these conditions in Figure 12. However, as just demonstrated, the nature of the irradiation effect is specific to the location of the charge transition levels for each point defect within the gap, and how these interact. If the anion vacancy preferred the neutral charge state across the majority of the gap (similar to the interstitial), an acceleration in transport kinetics would be seen instead. Other materials where thermal oxide growth is mediated by other defects will interact with space charge distributions in a different manner. Finally, conditions with a significant externally generated potential, such as from electro-chemical effects, could bias the flux of irradiation induced defects, and this effect could be significant for thinner films (lower temperatures) outside of the parabolic growth regime.

4. Discussion

This study has not considered internal clustering of point defects into large complexes and damage microstructures. Vacancies from opposite sublattices holding opposing charge will be driven by the Coloumb interaction to form di-vacancy pairs, larger clusters, and eventually voids. Similarly, interstitials aggregate into prismatic dislocation loops. Presumably, these features would prefer and stabilize charge neutral configurations in contrast to the preferences of isolated point defects. As such, the Fermi level shifts from monomer defects as reported here are best interpreted as an upper limit, and the response of a real material will likely be moderated by cluster formation.

The general reduction in transport kinetics for hematite in the reactor relevant temperature and dose rate regime cannot be easily generalized to other materials. The space charge that develops from irradiation induced defects is sensitive to the CTL for each defect, as demonstrated by modifying the properties of different types of vacancies. The balance between competing effects could easily shift in favor of accelerated corrosion for a different material with different charge transition levels.

Further, for oxides where significant internal charge develops under thermal corrosion conditions, superposition with radiation induced defects may follow different patterns than the ones seen here. In fact, the type of space charge which builds up from radiation induced defect supersaturations should be expected to be a delicate function of the specific defect properties of each oxide that can vary substantially between compounds, or even between nominally similar materials with different impurity/dopant content dictating the initial Fermi level.

Finally, the question of boundary conditions on the electrostatics problem has been left largely unaddressed here. The interior contact with magnetite has followed a contact barrier height consistent with the CNL of bulk material. This may well prove a poor assumption. However, we saw little to no difference to oxidation properties using a charge insulating interface instead. The interface may develop a strong charge dipole that would substantially shift the contact Fermi level one direction or the other, and the nature of that dipole itself might change substantially in an interface modified by irradiation. However, such an effect would be depleted within the Debye length, and parabolic behavior should be re-established once such a scale thickness is reached. A similar effect might be created by strongly charged adsorbed oxygen, which here has been treated as primarily charge neutral like the anion interstitial in bulk. The anticipated effect is similar, only modifying kinetics significantly for thin films and early times. Notably, the early behavior of iron oxidation does deviate from the parabolic rates of thicker films, and the direction of that deviation varies with temperature[85].

5. Conclusions

This work outlines a kinetic framework for simulating point defect transport in bulk oxides and through oxide scales growing on metals or other oxide phases. This approach is capable of directly interfacing with atomistic calculations of charged point defect formation and migration energetics. It's flexibility enable a wide range of potential applications ranging from irradiation effects on transport in functional oxides and predicting thermal and irradiation modified corrosion kinetics. In this study, our model was applied to hematite and closely reproduced a variety of properties including non-stoichiometry, diffusivity, and parabolic growth constants under thermal conditions.

The model was also applied to hematite in irradiation environments, predicting significant changes in bulk oxide properties. However, the nature of irradiation effects in bulk material were demonstrated to be quite different from those in oxide scales formed during corrosion. Principally, This work demonstrates that radiation enhanced diffusion RED - even when many order of magnitude faster than thermal self-diffusion in bulk material - cannot accelerate corrosion kinetics meaningfully on its own. However, radiation induced defects can shift the Fermi level and establish electrostatic potentials that alter net defect current, modify dominant charge states for defects, and thereby influence corrosion kinetics. For hematite scales, vacancy properties as reported in existing literature promote slower oxidation due internal charge accumulation from radiation induced vacancies that unfavorably impacts cation interstitial transport through hematite layers.

6. Acknowledgments

This work was supported as part of FUTURE (Fundamental Understanding of Transport Under Reactor Extremes), an Energy Frontier Research Center funded by the U.S. Department of Energy, Office of Science, Basic Energy Sciences.

7. Data availability

The data used in this paper will be made available by the authors upon reasonable request.

Appendix A. Electrostatic potential from internal defects

The electrostatic potential can be divided into two separate parts via the superposition principle. The first is governed by the distribution of charges internal to the oxide scale. The spatial variation in electric field $E = -\nabla\phi$ follows

$$\nabla \cdot E = \frac{\rho}{\epsilon}. \tag{A.1}$$

The second component is created by an unknown distribution of external charges. This contribution to the field must be uniform and constant within the oxide, and will be written here as E_{ext}. The internal charge density can be divided into uniform and spatially varying components

$$\bar{\rho} = \frac{1}{L}\int_0^L \rho(x)dx \tag{A.2}$$

$$\tilde{\rho}(x) = \rho(x) - \bar{\rho} \tag{A.3}$$

the first of which determines the difference in field at each edge of the scale, but cannot create a potential difference. The potential drop across a scale of thickness L due to internal charges is then given by

$$\Delta\phi = -\int_0^L \int_0^x \frac{\tilde{\rho}(\xi)}{\epsilon} d\xi dx \tag{A.4}$$

which integrates by parts to produce

$$\Delta\phi = \int_0^L \frac{(x - L/2)\,\rho(x)}{\epsilon} dx \tag{A.5}$$

which is the first moment of the charge density. This acts in addition to any externally applied field E_{ext}, which is an environmental parameter independent of the charge distribution in the oxide itself.

Midgap Formation Energy (eV)						
Charge	V_O	V_{Fe}	O_i	Fe_i	n	p
0	3.46	3.16	2.28	4.88	0.00	0.00
1	3.39	2.20	4.81	4.56	0.65	1.10
2	3.44	2.68	2.89	4.38	n/a	n/a
3	n/a	0.80	n/a	4.84	n/a	n/a
Migration Energy (eV)						
Charge	V_O	V_{Fe}	O_i	Fe_i		
0	1.30	2.12	0.46	2.41		
1	1.18	2.05	n/a	1.46		
2	1.24	1.33	0.44	0.81		
3	n/a	1.48	n/a	0.64		

Table B.2: Point defect formation and migration energies by charge state. Charges are positive for V_O and Fe_i and negative for V_{Fe} and O_i. For polarons, charge 0 indicates the absence of a polaron, while charge 1 represents the localization of a single carrier to an atom.

Appendix B. Defect thermodynamics

Defect formation and migration energies for hematite have been reported previously[75]. For self-consistency, we use the data reported by Banerjee, also shown in Table B.2. Migration barriers are given for each charge state, as well the mid gap formation energy against O_2 gas at STP. Also shown is the relevant polaron levels used in this work, where the electron polaron was reported by Lee and Han[48].

Notably, certain charge states are highly unfavorable, and do not appear on the convex hulls, plotted in figure B.15. Namely, O_i' and V_{Fe}'' do not appear, and are notably both charge +1 with respect to the full formal charge. Similarly, the hole polaron is difficult to localize in isolation. In the simplest analysis, this all aligns well with the high cost of localizing a single positive charge to form either Fe^{4+} or O^{1-} among the defect's neighbor atoms. The relative ease of creating Fe^{2+} renders the full range of n-type defect charge states easier to attain.

Aligning the DFT reference oxygen level to data recorded in thermochemistry tables was treated as a fitting parameter (as described in section 2.7), as were defect mobility prefactors. These were selected by linear regression against the empirical data included in Figure 5, and are listed in Table B.3. Separate regressions were done for cases including and excluding polaron states, with slight differences between the two. The mobility prefactor for V_{Fe} had no influence on observable properties within the physically relevant range. Additional material parameters for hematite are given in Table B.4.

		With Polaron	Without Polaron
ζ	(eV)	0.227	0.042
$S^f[V_O]$	(k_b)	0.63	2.59
$D_0[V_O]$	(m^2/s)	2.39×10^{-7}	1.05×10^{-7}
$D_0[O_i]$	(m^2/s)	1.29×10^{-5}	7.74×10^{-5}
$D_0[Fe_i]$	(m^2/s)	2.81×10^{-4}	4.58×10^{-3}

Table B.3: Fitted O_2 alignment parameter ζ and point defect properties for models including and excluding polaron states. Cation vacancy parameters had no effect on fit quality in the physically relevant range.

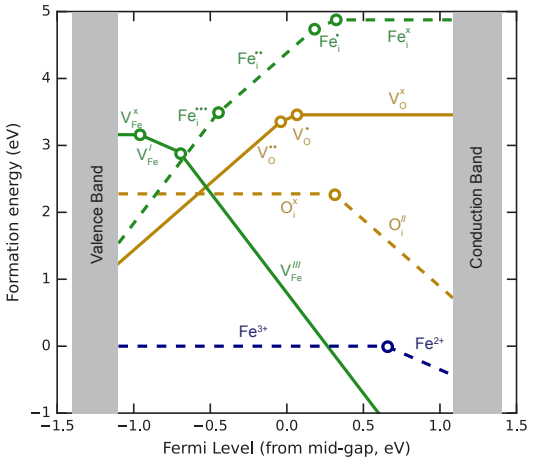

Figure B.15: Convex hulls for point defect and polaron formation energies in Hematite referenced to O_2 (uncorrected) in DFT.

Parameter	Value	Unit
Dielectric constant (ϵ)	23.67	ϵ_0
Anion site density (c_O^0)	62.0	nm^{-3}
Cation site density (c_{Fe}^0)	41.4	nm^{-3}
Reaction radius (r_{AB})	0.60	nm
Effective mass (m_n^*, m_p^*)	1	
Band Gap (E_g)	2.2	eV
Production efficiency (η)	0.1	

Table B.4: Additional material properties for hematite required for the cluster dynamics models. Dielectric constant, lattice densities, and bandgap were taken from the same DFT calculations as the defect energetics, other parameters are assumed or empirical.

Appendix C. Radiation Enhanced Diffusion

Here we produce the expressions for the recombination and sink limited cases for radiation enhanced diffusion. The net self-diffusion is given by the sum of interstitial and vacancy mediated transport

$$D^{\mathrm{RED}} = \frac{1}{c_0}\left(D_i c_i + D_v c_v\right) \tag{C.1}$$

and the homogenized steady state concentrations are given by

$$0 = g - D_i k^2 c_i - k_{iv} c_i c_v \tag{C.2}$$

$$0 = g - D_v k^2 c_v - k_{iv} c_i c_v \tag{C.3}$$

$$k_{iv} = 4\pi r_{iv}\left(D_i + D_v\right) \tag{C.4}$$

including loss to sinks and recombination. In the limit that recombination is negligible, the concentrations are given trivially by

$$c_i = g/D_i k^2 \tag{C.5}$$

$$c_v = g/D_v k^2. \tag{C.6}$$

When inserted into Eq (C.1), the diffusivities cancel and self-diffusion becomes

$$D^{\mathrm{RED}} = \frac{2g}{c_0 k^2} \tag{C.7}$$

which has no explicit temperature dependence.

As recombination becomes more prevalent, the solution to Eq (C.2) becomes

$$c_i = D_v k^2 \alpha / 2k_{iv} \tag{C.8}$$

$$c_v = D_i k^2 \alpha / 2k_{iv} \tag{C.9}$$

$$D^{RED} = D_i D_v k^2 \alpha / c_0 k_{iv} \tag{C.10}$$

instead, with

$$\alpha = \left(1 + \frac{4gk_{iv}}{D_i D_v k^4}\right)^{1/2} - 1 \tag{C.11}$$

defining the balance between loss to sinks and recombination. The two limiting expressions for alpha are

$$\alpha \approx \begin{cases} \frac{2gk_{iv}}{k^4 D_i D_v} & k^4 D_i D_v >> gk_{iv} \\ \left(\frac{4gk_{iv}}{k^4 D_i D_v}\right)^{1/2} & k^4 D_i D_v << gk_{iv} \end{cases} \tag{C.12}$$

for sink and recombination limited cases, respectively. The former reduces to Eq (C.7), while the latter gives

$$D^{\mathrm{RED}} \approx \frac{D_i D_v k^2}{c_0 k_{iv}} \left(\frac{4gk_{iv}}{D_i D_v k^4}\right)^{1/2} \tag{C.13}$$

The recombination rate coefficient k_{iv} is governed by the diffusivity of the faster species (interstitials in hematite), and the self diffusion becomes

$$D^{\mathrm{RED}} = \left(\frac{D_v g}{\pi r_{iv}}\right)^{1/2} \tag{C.14}$$

which is equivalent to Eq (41) in the main text.

When no sinks at all are present, defects can only recombine, such that their concentrations must be identical in order to conserve mass. The steady state concentration of both defects is then given by

$$c_{i/v} = \left(\frac{g}{k_{iv}}\right)^{1/2} \tag{C.15}$$

with self diffusion given by

$$D^{\mathrm{RED}} \approx \frac{1}{c_0} \left(\frac{gD_i}{4\pi r_{iv}}\right)^{1/2} \tag{C.16}$$

but this limit was never realized in this study, even up to 10 μm oxide films.

References

[1] J.-C. Boivin, Structural and electrochemical features of fast oxide ion conductors, International Journal of Inorganic Materials 3 (8) (2001) 1261–1266.

[2] J. Kim, S. J. Pearton, C. Fares, J. Yang, F. Ren, S. Kim, A. Y. Polyakov, Radiation damage effects in ga 2 o 3 materials and devices, Journal of Materials Chemistry C 7 (1) (2019) 10–24.

[3] C. Matthews, R. Perriot, M. W. Cooper, C. R. Stanek, D. A. Andersson, Cluster dynamics simulation of uranium self-diffusion during irradiation in uo2, Journal of Nuclear Materials 527 (2019) 151787.

[4] A. Couet, A. T. Motta, R. J. Comstock, Hydrogen pickup measurements in zirconium alloys: Relation to oxidation kinetics, Journal of Nuclear Materials 451 (1-3) (2014) 1–13.

[5] A. Atkinson, Transport processes during the growth of oxide films at elevated temperature, Reviews of Modern Physics 57 (2) (1985) 437.

[6] N. Cabrera, N. F. Mott, Theory of the oxidation of metals, Reports on progress in physics 12 (1) (1949) 163.

[7] F. P. Fehlner, N. F. Mott, Low-temperature oxidation, Oxidation of metals 2 (1) (1970) 59–99.

[8] C. Chao, L. Lin, D. D. Macdonald, A point defect model for anodic passive films: I. film growth kinetics, Journal of the Electrochemical Society 128 (6) (1981) 1187.

[9] D. D. Macdonald, The history of the point defect model for the passive state: a brief review of film growth aspects, Electrochimica Acta 56 (4) (2011) 1761–1772.

[10] A. Seyeux, V. Maurice, P. Marcus, Oxide film growth kinetics on metals and alloys: I. physical model, Journal of The Electrochemical Society 160 (6) (2013) C189.

[11] C. Wagner, Beitrag zur theorie des anlaufvorgangs, Zeitschrift für physikalische Chemie 21 (1) (1933) 25–41.

[12] G. Marsh, K. Taylor, G. Bryan, S. Worthington, The influence of radiation on the corrosion of stainless steel, Corrosion science 26 (11) (1986) 971–982.

[13] M. Boisson, L. Legras, E. Andrieu, L. Laffont, Role of irradiation and irradiation defects on the oxidation first stages of a 316l austenitic stainless steel, Corrosion Science 161 (2019) 108194.

[14] F. Schmidt, P. Hosemann, R. O. Scarlat, D. K. Schreiber, J. R. Scully, B. P. Uberuaga, Effects of radiation-induced defects on corrosion, Annual Review of Materials Research 51 (1) (2021) 293–328.

[15] R. Lillard, D. Pile, D. Butt, The corrosion of materials in water irradiated by 800 mev protons, Journal of nuclear materials 278 (2-3) (2000) 277–289.

[16] G. Was, C.-B. Bahn, J. Busby, B. Cui, D. Farkas, M. Gussev, M. R. He, J. Hesterberg, Z. Jiao, D. Johnson, et al., How irradiation promotes intergranular stress corrosion crack initiation, Progress in Materials Science 143 (2024) 101255.

[17] S. S. Raiman, G. S. Was, Accelerated corrosion and oxide dissolution in 316l stainless steel irradiated in situ in high temperature water, Journal of Nuclear Materials 493 (2017) 207–218.

[18] M. Reyes, A. Aryanfar, S. W. Baek, J. Marian, Multilayer interface tracking model of zirconium clad oxidation, Journal of Nuclear Materials 509 (2018) 550–565.

[19] M. Reyes, P. Wang, G. Was, J. Marian, Determination of dose rate effects on zircaloy oxidation using proton irradiation and oxygen transport modeling, Journal of Nuclear Materials 523 (2019) 56–65.

[20] P. Hosemann, R. Greco, I. Usov, Y. Wang, S. Maloy, N. Li, The design, setup and operational testing of the irradiation and corrosion experiment (ice), Journal of nuclear materials 376 (3) (2008) 392–395.

[21] R. Klueh, D. Gelles, S. Jitsukawa, A. Kimura, G. Odette, B. Van der Schaaf, M. Victoria, Ferritic/martensitic steels–overview of recent results, Journal of Nuclear Materials 307 (2002) 455–465.

[22] R. Klueh, A. T. Nelson, Ferritic/martensitic steels for next-generation reactors, Journal of nuclear materials 371 (1-3) (2007) 37–52.

[23] A.-A. Tavassoli, E. Diegele, R. Lindau, N. Luzginova, H. Tanigawa, Current status and recent research achievements in ferritic/martensitic steels, Journal of Nuclear Materials 455 (1-3) (2014) 269–276.

[24] S. Das, S. Sanyal, P. Halder, A. Varma, Y. Ravi Kumar, S. Mandal, Oxide scale characterization and study of oxidation kinetics in t91 steel exposed to dry air at high temperatures (873–1073 k), Metals and Materials International (2022) 1–17.

[25] C. Liu, L. Qi, T. Shen, P. Jin, Z. Wang, Tem comparative study on oxide films of 316l and t91 steel exposed to 350–500° c steam, Journal of Materials Science & Technology 175 (2024) 10–21.

[26] S. Fetni, D. Montero, C. Boubahri, D. Brouri, J. Briki, Evolution mechanisms of t91 steel in subcritical conditions and role of an internal oxidation zone, Oxidation of Metals 90 (2018) 291–315.

[27] Z. Zhu, H. Xu, D. Jiang, X. Mao, N. Zhang, Influence of temperature on the oxidation behaviour of a ferritic-martensitic steel in supercritical

water, Corrosion Science 113 (2016) 172–179.
[28] D. Frazer, S. Qvist, S. Parker, D. Krumwiede, M. Caro, J. Tesmer, S. Maloy, Y. Wang, P. Hosemann, Degradation of ht9 under simultaneous ion beam irradiation and liquid metal corrosion, Journal of Nuclear Materials 479 (2016) 382–389.
[29] A. Atkinson, R. Taylor, Diffusion of 55fe in fe2o3 single crystals, Journal of Physics and Chemistry of Solids 46 (4) (1985) 469–475.
[30] K. Reddy, A. R. Cooper, Oxygen diffusion in mgo and α-fe2o3, Journal of the American Ceramic Society 66 (9) (1983) 664–666.
[31] B. Amami, M. Addou, F. Millot, A. Sabioni, C. Monty, Self-diffusion in α-fe 2 o 3 natural single crystals, Ionics 5 (1999) 358–370.
[32] A. Sabioni, A.-M. Huntz, A. Daniel, W. Macedo, Measurement of iron self-diffusion in hematite single crystals by secondary ion-mass spectrometry (sims) and comparison with cation self-diffusion in corundum-structure oxides, Philosophical Magazine 85 (31) (2005) 3643–3658.
[33] K. Hoshino, N. Peterson, Cation self-diffusion and the isotope effect in fe2o3, Journal of Physics and Chemistry of Solids 46 (3) (1985) 375–382.
[34] R. Dieckmann, Point defects and transport in haematite (fe2o3-ε), Philosophical Magazine A 68 (4) (1993) 725–745.
[35] A. Polyakov, N. Smirnov, A. Govorkov, A. Markov, N. Kolin, D. Merkurisov, V. Boiko, K. Shcherbatchev, V. Bublik, M. Voronova, et al., Fermi level pinning in heavily neutron-irradiated gan, Journal of applied physics 100 (9) (2006).
[36] W. Walukiewicz, Mechanism of fermi-level stabilization in semiconductors, Physical Review B 37 (9) (1988) 4760.
[37] M. Singh, T. Kumagai, A. El-Azab, A first-principles investigation of point defect structure and energetics in tho2, Journal of Applied Physics 132 (13) (2022).
[38] A. A. Kohnert, B. D. Wirth, L. Capolungo, Modeling microstructural evolution in irradiated materials with cluster dynamics methods: A review, Computational Materials Science 149 (2018) 442–459.
[39] T. Jourdan, G. Bencteux, G. Adjanor, Efficient simulation of kinetics of radiation induced defects: A cluster dynamics approach, Journal of Nuclear Materials 444 (1-3) (2014) 298–313.
[40] J. Marian, V. V. Bulatov, Stochastic cluster dynamics method for simulations of multispecies irradiation damage accumulation, Journal of Nuclear Materials 415 (1) (2011) 84–95.
[41] J. Yu, X.-M. Bai, A. El-Azab, T. R. Allen, Oxygen transport in off-stoichiometric uranium dioxide mediated by defect clustering dynamics, The Journal of Chemical Physics 142 (9) (2015).
[42] S. K. Mazumder, M. K. S. Singh, T. Kumagai, A. El-Azab, Atomistically-informed modeling of point defect clustering and evolution in irradiated tho2, Chemical Physics 562 (2022) 111645.
[43] W. R. Wampler, S. M. Myers, Model for transport and reaction of defects and carriers within displacement cascades in gallium arsenide, Journal of Applied Physics 117 (4) (2015).
[44] M. Smoluchowski, Mathematical theory of the kinetics of the coagulation of colloidal solutions, Z. Phys. Chem. 92 (1917) 129–168.
[45] T. Waite, General theory of bimolecular reaction rates in solids and liquids, The Journal of Chemical Physics 28 (1) (1958) 103–106.
[46] A. Alkauskas, Q. Yan, C. G. Van de Walle, First-principles theory of nonradiative carrier capture via multiphonon emission, Physical Review B 90 (7) (2014) 075202.
[47] C. N. Singh, B. P. Uberuaga, S. J. Tobin, X.-Y. Liu, Impact of radiation-induced point defects on thermal carrier decay processes in gaas, Acta Materialia 242 (2023) 118480.
[48] J. Lee, S. Han, Thermodynamics of native point defects in α-fe 2 o 3: an ab initio study, Physical Chemistry Chemical Physics 15 (43) (2013) 18906–18914.
[49] T. J. Smart, Y. Ping, Effect of defects on the small polaron formation and transport properties of hematite from first-principles calculations, Journal of Physics: Condensed Matter 29 (39) (2017) 394006.
[50] C. Lohaus, A. Klein, W. Jaegermann, Limitation of fermi level shifts by polaron defect states in hematite photoelectrodes, Nature communications 9 (1) (2018) 4309.
[51] N. Ansari, K. Ulman, M. F. Camellone, N. Seriani, R. Gebauer, S. Piccinin, Hole localization in fe 2 o 3 from density functional theory and wave-function-based methods, Physical Review Materials 1 (3) (2017) 035404.
[52] A. Braun, Q. Chen, D. Flak, G. Fortunato, K. Gajda-Schrantz, M. Grätzel, T. Graule, J. Guo, T.-W. Huang, Z. Liu, et al., Iron resonant photoemission spectroscopy on anodized hematite points to electron hole doping during anodization, ChemPhysChem 13 (12) (2012) 2937–2944.
[53] K. M. Rosso, D. M. Smith, M. Dupuis, An ab initio model of electron transport in hematite (α-fe 2 o 3) basal planes, The Journal of chemical physics 118 (14) (2003) 6455–6466.
[54] C. S. Ahart, J. Blumberger, K. M. Rosso, Polaronic structure of excess electrons and holes for a series of bulk iron oxides, Physical Chemistry Chemical Physics 22 (19) (2020) 10699–10709.
[55] R. Eymard, T. Gallouët, R. Herbin, Finite volume methods, Handbook of numerical analysis 7 (2000) 713–1018.
[56] F. Moukalled, L. Mangani, M. Darwish, F. Moukalled, L. Mangani, M. Darwish, The finite volume method, Springer, 2016.
[57] K. Nordlund, S. J. Zinkle, A. E. Sand, F. Granberg, R. S. Averback, R. E. Stoller, T. Suzudo, L. Malerba, F. Banhart, W. J. Weber, et al., Primary radiation damage: A review of current understanding and models, Journal of Nuclear Materials 512 (2018) 450–479.
[58] R. T. Tung, Recent advances in schottky barrier concepts, Materials Science and Engineering: R: Reports 35 (1-3) (2001) 1–138.
[59] S. Zhang, J. E. Northrup, Chemical potential dependence of defect formation energies in gaas: Application to ga self-diffusion, Physical review letters 67 (17) (1991) 2339.
[60] Y. Kumagai, F. Oba, Electrostatics-based finite-size corrections for first-principles point defect calculations, Physical Review B 89 (19) (2014) 195205.
[61] C. Freysoldt, J. Neugebauer, C. G. Van de Walle, Electrostatic interactions between charged defects in supercells, physica status solidi (b) 248 (5) (2011) 1067–1076.
[62] E. Clouet, C. Varvenne, T. Jourdan, Elastic modeling of point-defects and their interaction, Computational Materials Science 147 (2018) 49–63.
[63] E. Sargeant, F. Illas, P. Rodriguez, F. Calle-Vallejo, Importance of the gas-phase error correction for o2 when using dft to model the oxygen reduction and evolution reactions, Journal of Electroanalytical Chemistry 896 (2021) 115178.
[64] S. Grindy, B. Meredig, S. Kirklin, J. E. Saal, C. Wolverton, Approaching chemical accuracy with density functional calculations: Diatomic energy corrections, Physical Review B—Condensed Matter and Materials Physics 87 (7) (2013) 075150.
[65] Y. Zhang, D. A. Kitchaev, J. Yang, T. Chen, S. T. Dacek, R. A. Sarmiento-Pérez, M. A. Marques, H. Peng, G. Ceder, J. P. Perdew, et al., Efficient first-principles prediction of solid stability: Towards chemical accuracy, npj Computational Materials 4 (1) (2018) 9.
[66] M. Kothakonda, A. D. Kaplan, E. B. Isaacs, C. J. Bartel, J. W. Furness, J. Ning, C. Wolverton, J. P. Perdew, J. Sun, Testing the r2scan density functional for the thermodynamic stability of solids with and without a van der waals correction, ACS Materials Au 3 (2) (2022) 102–111.
[67] K. Reuter, M. Scheffler, Composition, structure, and stability of ruo 2 (110) as a function of oxygen pressure, Physical Review B 65 (3) (2001) 035406.
[68] L. Wang, T. Maxisch, G. Ceder, Oxidation energies of transition metal oxides within the gga+ u framework, Physical Review B—Condensed Matter and Materials Physics 73 (19) (2006) 195107.
[69] A. Jain, G. Hautier, S. P. Ong, C. J. Moore, C. C. Fischer, K. A. Persson, G. Ceder, Formation enthalpies by mixing gga and gga+ u calculations, Physical Review B—Condensed Matter and Materials Physics 84 (4) (2011) 045115.
[70] A. Wang, R. Kingsbury, M. McDermott, M. Horton, A. Jain, S. P. Ong, S. Dwaraknath, K. A. Persson, A framework for quantifying uncertainty in dft energy corrections, Scientific reports 11 (1) (2021) 15496.
[71] M. W. Chase, Nist-janaf thermochemical tables 4th ed., J. of Physical and Chemical Reffernce Data (1998) 1529–1564.
[72] G. Henkelman, B. P. Uberuaga, H. Jónsson, A climbing image nudged elastic band method for finding saddle points and minimum energy paths, The Journal of chemical physics 113 (22) (2000) 9901–9904.
[73] A. Banerjee, A. A. Kohnert, E. F. Holby, B. P. Uberuaga, Critical assessment of the thermodynamics of vacancy formation in fe2o3 using hybrid density functional theory, The Journal of Physical Chemistry C 124 (43) (2020) 23988–24000.
[74] A. Banerjee, A. A. Kohnert, E. F. Holby, B. P. Uberuaga, Interplay between defect transport and cation spin frustration in corundum-structured oxides, Physical Review Materials 5 (3) (2021) 034410.

[75] A. Banerjee, E. F. Holby, A. A. Kohnert, S. Srivastava, M. Asta, B. P. Uberuaga, Thermokinetics of point defects in α-fe2o3, Electronic Structure 5 (2) (2023) 024007.
[76] T. C. Kaspar, S. D. Taylor, K. H. Yano, T. G. Lach, Y. Zhou, Z. Zhu, A. A. Kohnert, E. K. Still, P. Hosemann, S. R. Spurgeon, et al., Bulk and short-circuit anion diffusion in epitaxial fe2o3 films quantified using buried isotopic tracer layers, Advanced Materials Interfaces 8 (9) (2021) 2001768.
[77] K. H. Yano, A. A. Kohnert, A. Banerjee, D. J. Edwards, E. F. Holby, T. C. Kaspar, H. Kim, T. G. Lach, S. D. Taylor, Y. Wang, et al., Radiation-enhanced anion transport in hematite, Chemistry of Materials 33 (7) (2021) 2307–2318.
[78] J. Buckeridge, Equilibrium point defect and charge carrier concentrations in a material determined through calculation of the self-consistent fermi energy, Computer Physics Communications 244 (2019) 329–342.
[79] E. J. Caule, K. Buob, M. Cohen, Oxidation of iron in the temperature range of 260–470° c, Journal of The Electrochemical Society 108 (9) (1961) 829.
[80] D. Channing, M. Graham, A study of iron oxidation processes by mössbauer spectroscopy, Corrosion science 12 (3) (1972) 271–289.
[81] D. Channing, S. Dickerson, M. Graham, A study of the growth of iron oxides by mössbauer spectroscopy, Corrosion Science 13 (12) (1973) 933–938.
[82] G. S. Was, Fundamentals of radiation materials science: metals and alloys, Springer, 2007.
[83] K. H. Yano, A. A. Kohnert, T. C. Kaspar, S. D. Taylor, S. R. Spurgeon, H. Kim, Y. Wang, B. P. Uberuaga, D. K. Schreiber, Dose rate dependent cation & anion radiation enhanced diffusion in hematite, Journal of Materials Chemistry A 10 (45) (2022) 24167–24177.
[84] L. Mansur, Theory of transitions in dose dependence of radiation effects in structural alloys, Journal of nuclear materials 206 (2-3) (1993) 306–323.
[85] D. Caplan, M. Cohen, Effect of cold work on the oxidation of iron from 400–650° c, Corrosion Science 6 (7) (1966) 321–335.

Highlights

- Developed a new kinetic model for oxide growth kinetics in extreme environments
- Directly informed by point defect energetics from density functional theory
- Reproduces observed macroscopic properties of Hematite
- Predicts changes in oxidation kinetics and self-diffusion due to irradiation

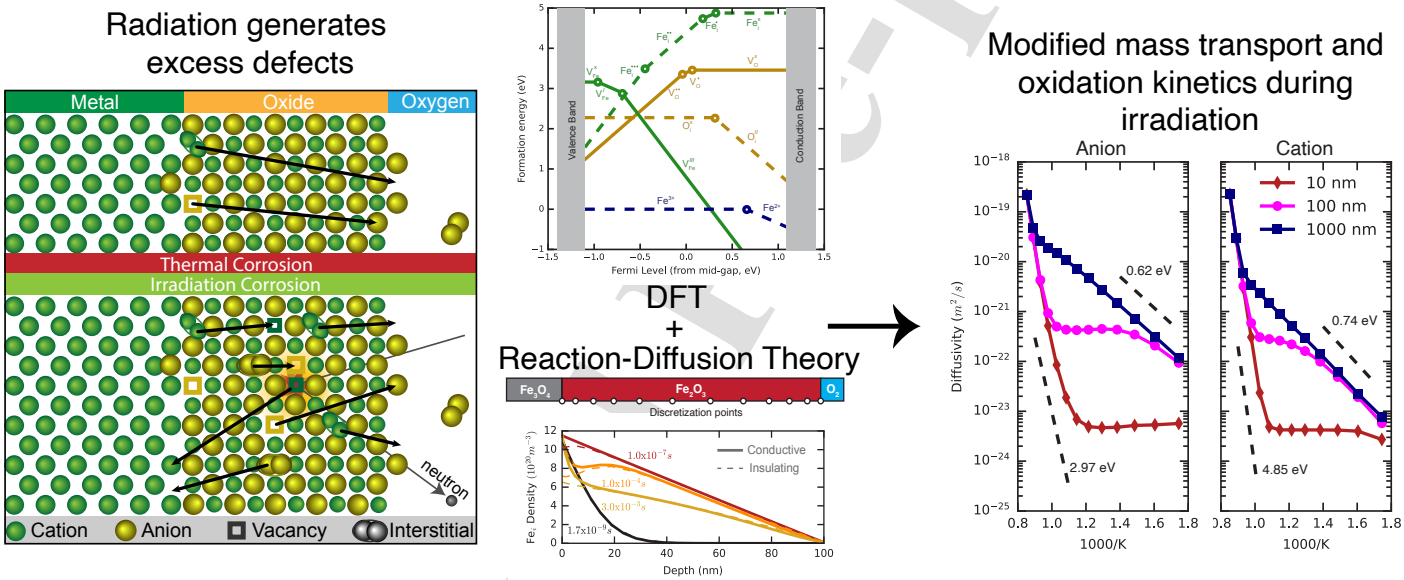

Aaron Kohnert: Conceptualization, Methodology, Investigation, Software, Writing **Edward Holby**: Methodology, Writing **Elizabeth Peterson**: Methodology, Writing **Shivani Srivastava**: Methodology, Writing **Mark Asta**: Conceptualization, Methodology **Blas Uberuaga**: Conceptualization, Methodology, Funding Acquisition

Declaration of interests

☐ The authors declare that they have no known competing financial interests or personal relationships that could have appeared to influence the work reported in this paper.

☒ The authors declare the following financial interests/personal relationships which may be considered as potential competing interests:

Aaron Kohnert reports financial support was provided by US Department of Energy Basic Energy Sciences. If there are other authors, they declare that they have no known competing financial interests or personal relationships that could have appeared to influence the work reported in this paper.